

Custom Mass Ranging Extension 2.0

Ty J. Prosa

May 8, 2025

The “CustomMassRanging” extension provides an automated re-ranging scheme of existing IVAS ranges. An adjacent-to-peak background estimation is used based on the initial list of ions and ranges provided by IVAS. Adding or deleting ion ranges must be done in IVAS, before passing them on to this extension. A peak discovery feature displays found peaks, but is currently for visualization only (expected in 3.0).

Input: A set of pre-defined ion ranges from a normal IVAS session.

Extension Function: Four ranging schemes are available: Left, Half, Quarter, and LeftTail. The extension auto-determines which of the first three schemes is appropriate on a peak-by-peak basis. The user can override the scheme for any given peak, and choose the LeftTail option, which attempts to fit the tail of the peak with a decaying exponential fit or unranged regions in the tail. Ionic and decomposed ion bulk compositions are then determined with full statistical consideration for detection threshold and resulting compositional uncertainty. When using the LeftTail option, the user specifies their estimated uncertainty in the tail estimate and that error is also propagated to the bulk compositions.

Output: Background estimates are displayed on the mass histogram as well as any tail estimate (and all discovered peaks). The user can then choose to pass/apply new ion ranges back to IVAS or change ranging parameters and re-range again. The utilized extension parameters, those from the last apply operation, are saved as part of any subsequent “save analysis tree” operation.

Details

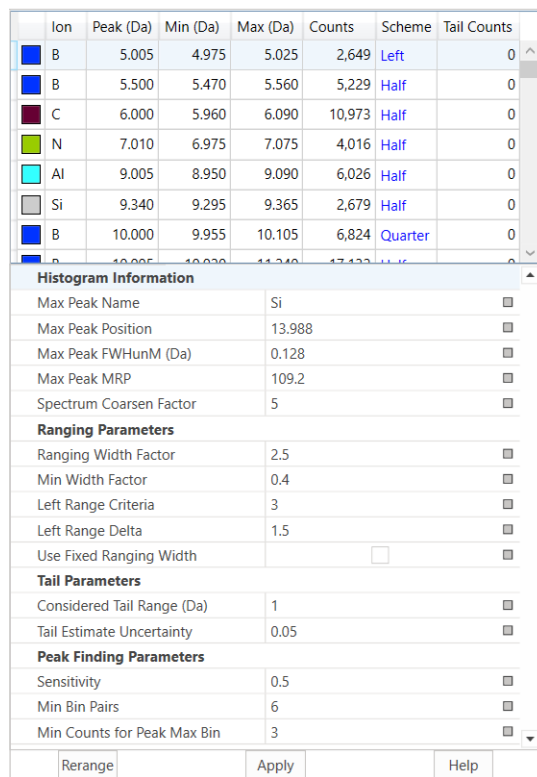
The initial ion list and range definitions are the RRNG-type data passed from IVAS, and the range list items cannot be added to or deleted within the extension (the user needs to do that in IVAS and then pass that list to the extension). The ranging procedure is consistent with the analysis described in Prosa and Oltman, 2022 (attached at end):

Overlapping initial range definitions are not allowed (although the starting IVAS version does allow). An exception will be generated and the user notified when input ranges have overlaps.

- 1) The most intense histogram bin in the mass spectrum is discovered and processed for peak m/z position and full-width-hundredth max (FWHunM, note in the

publication, the FW0.001M was used, but that metric may not sufficiently robust for general mass spectra).

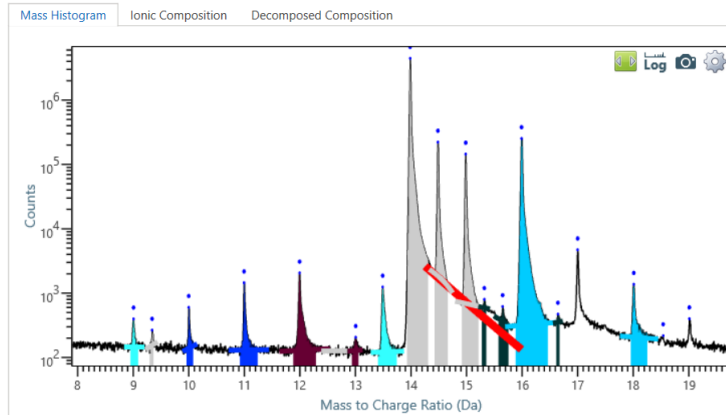
- 2) FWHunM is used to determine the histogram m/z resolution. Typically, the input mass histogram has a resolution of 0.001 Da. The algorithm coarsens the resolution so that 15-30 bins encompass the FWHunM of the main peak (typically, somewhere between 0.002 Da to 0.01 Da).
- 3) The peaks are processed from left to right along the mass spectrum to determine the appropriate ranging scheme. Ideally, a background range of the same width as the ranged peak is used to estimate the background for a given peak. The scheme is determined as follows: If there are no peaks defined within a certain distance to the left of a given peak (as defined by “Left Range Criteria”), then the Left ranging scheme will be used. That is, a range defined at some specified distance to the left (as defined by “Left Range Delta”) of the given peak and the same width. If the left-ranging criteria fail, then an evaluation is made for nearest peaks on either side of the given peak. Nearest peak >0.9 Da away is the criteria for a Half-width ranging scheme. Immediately adjacent to the left and right of a prospective peak range, background ranges of half the prospective peak range width are defined and used to estimate the background. The Half scheme is equivalent to estimating a linear background correction for that peak. Otherwise, the Quarter-width ranging scheme is used. Same as the Half scheme, except background counts need to be doubled to account for the range width and provide a linear background correction (and consequently the background uncertainty will be doubled as well).
- 4) Optimum ranges are determined given the initial ion range definitions and auto-determined schemes as follows:
 - a. A minimum range-width is defined based on the FWHunM.
 - b. The local maximum is determined for each initial ion range.
 - c. Left-scheme peaks use a fixed range width as specified in Parameters. The position of the fixed-width range is adjusted to yield the maximum number of total/net counts, and a same-width range is defined to the left of this peak (as specified in Parameters) as a background estimate.



d. For half-width and quarter-width schemes, the minimum range-width is positioned so that the net counts (total counts in ion range, minus the immediately adjacent background estimate) is maximum. Then the prospective range width is expanded 2 bins (or 4 bins for quarter-width ranging) at a time and re-evaluated. The process stops when the net counts begin to decrease.

e. Background ranging lines are added to the mass spectrum histogram. Note they are lines in linear-scale but curved in log-scale.

f. LeftTail performs an exponential fit to the ToF tail ($\sqrt{m/z}$).



Starting at the range maximum point and continuing for “Considered Tail Range”, ignoring any values defined by other ranges, these points are fit to an exponential function and those estimated counts are added to the various tables. Should the exponent be non-negative or span more than 5 Da before intersecting with the background, then the tail is rejected. The user specifies “Tail Estimate Uncertainty” as a fraction of the total number of counts. A value between 0.01 and 0.1 might be reasonable (1% and 10%). This uncertainty estimate and is propagated to the final composition results.

Mass Histogram							Ionic Composition							Decomposed Composition						
Ion	Composition	Sigma/DT (95% CL)	Counts	Background	Net	Tail	Element	Composition	Sigma/DT (%)	Counts	Background	Net	Tail							
Si	83.187%	0.028%	23,587,420	178,753	23,629,359	217,382	Si	80.881%	0.027%	25,020,914	331,709	24,936,735	243,588							
O	5.9438%	0.0044%	1,738,326	50,207	1,688,338	0	O	12.8237%	0.0070%	4,272,981	347,773	3,953,734	26,206							
SiO ₂	2.4268%	0.0030%	766,703	77,941	689,343	0	Co	2.0865%	0.0026%	687,877	44,677	643,304	0							
Ca	2.2346%	0.0028%	662,016	27,376	634,744	0	Ti	1.9679%	0.0029%	774,316	168,955	606,721	0							
SiO	1.9812%	0.0052%	574,335	37,787	562,757	26,206	Ge	1.4647%	0.0023%	510,312	59,169	451,579	0							
Ge	1.5898%	0.0025%	510,312	59,169	451,579	0	N	0.3978%	0.0013%	159,398	36,851	122,635	0							
TiO	1.0701%	0.0022%	379,190	76,041	303,963	0	C	0.1971%	0.0010%	108,640	48,149	60,777	0							
Ti	0.7554%	0.0021%	294,531	80,496	214,559	0	Al	0.09551%	0.00081%	58,894	29,608	29,448	0							
TiN	0.3105%	0.0011%	100,595	12,418	88,199	0	F	0.05301%	0.00055%	31,095	14,766	16,344	0							
C	0.08732%	0.00074%	43,452	18,888	24,803	0	B	0.01964%	0.00070%	45,831	39,828	6,054	0							
SiC	0.07234%	0.00065%	35,881	15,357	20,548	0	Hf	0.01302%	0.00038%	9,342	5,396	4,014	0							
Al	0.07061%	0.00075%	38,919	18,969	20,058	0	Au	-ND-	0.00069%	2,102	2,063	39	0							

- 5) Once the ranging definitions are finalized, ionic and decomposed ion compositions are calculated. For each range (or ion type) the net counts are evaluated for statistical significance (has a peak been detected with a 95% confidence level). Note that any Not Detected (-ND-) ranges are removed from composition

considerations and the 95% confidence level detection threshold is reported instead of sigma (the amount of that range/element that would be detected 95% of the time).

- 6) User must use the “Apply” button to transfer the new range definitions back to IVAS. The Parameters Table will then be transferred to the Properties area of AP Suite which is captured and can be restored via “Saved Analysis State.”
- 7) A version of the peak ranging algorithm is used to look for any net counts that statistically might be a peak. The minimum range size is used bin by bin, starting at 0.8 Da. When the net counts are greater than (99%CL-DT/ Sensitivity), this constitutes a discovered peak. The range position is adjusted to yield the maximum net counts for that peak, and then the search process continues starting at the far-right edge of the discovered peak’s range extent. Blue dots (limited by plotting options) are displayed on the mass histogram.

Parameters Table:

Histogram Information

- Max Peak Name: Ion range of found max histogram position
- Max Peak Position: Position of found max histogram position
- Max Peak FWHunM (Da): Full width 0.01 maximum of found max histogram position region
- Max Peak MRP: Mass Resolving Power = 1/FWHunM
- Spectrum Coarsen Factor: Binning of extension mass spectrum used (number times the IVAS Binning (default 0.001 Da), so 15-30 bins covering the FWHunM)

Ranging Parameters

- Ranging Width Factor: Number times FWHunM for left-ranging or fixed ranging
- Min Width Factor: Number times FWHunM for minimum range width
- Left Range Criteria: Required region empty of defined ranges for left-ranging
- Left Range Delta: Position left of peak to center left background range
- Use Fixed Ranging Width: Do not use auto-width ranging (use fixed ranged determined by Ranging Width Factor above)

Tail Parameters

- Considered Tail Range (Da): Range beyond right-range-edge to fit exponential tail
- Tail Estimate Uncertainty: User estimated fractional uncertainty of total tail counts

Peak Discovery Parameters

- Sensitivity: Number times FWHunM for left-ranging or fixed ranging
- Min Bin Pairs: Minimum bin width for peak evaluation in coarsened bin pairs
- Min Counts for Peak Max Bin: Discovered peaks must have a bin with at least this many counts

*Note: Minimum and Fixed Width Scaling: Generally, minimum and fixed peak widths scale in ToF (or $\sqrt{m/z}$) relative to the Max Peak, so only the Max Peak will have the specific values as set forth in the parameter table. Ranges to the left will be slightly more narrow, and those to the right more broad. Depending on parameter definitions, very low m/z peaks might require near zero-width minimums, so the “Min Bin Pairs” parameter prevents this.

Additional Notes:

1. "Rerange" can be done multiple times (needed when users change Parameters or modify any Schemes).
2. Select>Select-All and Copy/Paste functions should work on all tables (column headers are not captured in this operation). Export features have not been provided as Copy/Paste provides for this capability.
3. Double clicking in plot region will unzoom x-axis. A second time is needed to unzoom y-axis. Auto-y-axis scaling is not a current feature.
4. Table columns are also sortable by clicking the column header, but note to control precision display, some numerical columns are of type string, and these will not always sort in numerical order!
5. Quarter-width ranging will have slightly larger uncertainty because the background is scaled by a factor of two (greater background uncertainty).
6. Decomposed compositions error propagation means that any molecular ion with an element that has greater than one atom in the molecular formula (e.g., O in SiO₂) will result in a larger uncertainty because of the scaling of those counts in the decomposition calculation (not historically accounted for in this way in IVAS). This is almost always insignificant, but for materials with a significant fraction of multi-same-atomic molecular species, this could become significant.
7. Tool tips are available for many table column headers, Parameters, and Properties.
8. Any changes in the IVAS ranges associated with an active extension session will force an update of the extension (start from the beginning).
9. Save Analysis Tree saves the current parameters and schemes (those shown in the properties region, which are modified only after apply has been done). Using a Saved Analysis tree will also override auto-scheme (not shown in Properties) with the previously used scheme for any matching ranges (since a Saved Analysis Tree can be applied to a different dataset than the one from which the save was performed, the IVAS ranges/ions list may be different).

Original Article

Study of LEAP® 5000 Deadtime and Precision via Silicon Pre-Sharpened-Microtip™ Standard Specimens

Ty J. Prosa*  and Edward Oltman

CAMECA Instruments, Inc., 5470 Nobel Drive, Madison, WI 53711, USA

Abstract

Atom probe tomography (APT) is a technique that has expanded significantly in terms of adoption, dataset size, and quality during the past 15 years. The sophistication used to ensure ultimate analysis precision has not kept pace. The earliest APT datasets were small enough that deadtime and background considerations for processing mass spectrum peaks were secondary. Today, datasets can reach beyond a billion atoms so that high precision data processing procedures and corrections need to be considered to attain reliable accuracy at the parts-per-million level. This paper considers options for mass spectrum ranging, deadtime corrections, and error propagation as applied to an extrinsic-silicon standard specimen to attain agreement for silicon isotopic fraction measurements across multiple instruments, instrument types, and acquisition conditions. Precision consistent with those predicted by counting statistics is attained showing agreement in silicon isotope fraction measurements across multiple instruments, instrument platforms, and analysis conditions.

Key words: atom probe tomography, deadtime, pile-up, precision, time-of-flight mass spectrometry

(Received 10 February 2021; revised 24 May 2021; accepted 6 June 2021)

Introduction

Atom probe tomography (APT) is a three-dimensional imaging technique that provides chemical and spatial information at near-atomic scale using time-of-flight mass spectrometry (ToF-MS) (Larson et al., 2013; Miller & Forbes, 2014). Analysis is enabled by shaping the solid into a nano-needle (~100 nm apex diameter), so that a few kilovolt voltage difference between specimen and counter electrode establishes a surface electric field sufficient to extract and ionize surface atoms (referred to as field evaporation) (Müller, 1956). Modern electropolishing and focused ion-beam (FIB) specimen preparation methods are capable of readily achieving these shapes, reviews of which are available in the literature (Gault et al., 2012; Larson et al., 2013; Miller & Forbes, 2014; Prosa & Larson, 2017).

As APT has evolved, so has data quality and analyzed volumes. Early atom probes recorded datasets of $\sim 10^5$ events, so that the ToF-MS would present as individual peaks without significant background. To avoid detector deadtime issues (commonly referred to as “pile-up”), data were often collected at rates such that multiple-ion emissions during a single ToF pulse were statistically insignificant (Rolander & Andren, 1994; Miller, 2000), although some investigators did note deadtime-related inaccuracies and corrections (Tsong et al., 1978; Cerezo et al., 1984; Menand et al., 1988; Rolander & Andren, 1989). Precision consistent with counting statistics could be accomplished by simple

ranging of the mass spectrum to integrate the total counts for each peak, with no deadtime or background corrections. Even though the detectors were not 100% efficient, the technology was equally sensitive to all ions, and so no sensitivity corrections were necessary either. Composition results with errors estimated via Bernoulli trials were consistent with the reported precision (Miller, 2000).

Modern APT data quality and analyzed volumes force the field to push beyond these simple methods and consider next-order corrections for deadtime and background contributions to achieve the precision expected for datasets 10^3 times larger (Larson et al., 2013). The last few years have seen discussion within the APT community for standardizing approaches to ranging and background correction because dispersion in reported results will depend on the validity and consistency of these approaches (Nakamura, 1986; Prosa et al., 2013b; Marquis et al., 2016; Exertier et al., 2018; Meisenkothen et al., 2020a). Likewise, deadtime considerations also become much more important (Lewis et al., 2015; Stephan et al., 2015). Even though low detection rates should minimize the likelihood of multi-ion-emission events, field evaporation physics yields event statistics that are neither random in time nor space, so purely analytical deadtime corrections are not possible, and this issue is a subject for this article.

Several examples of materials that present APT composition deficiencies have been reported in the literature. They expose applications where some aspect of unique evaporation physics conspires to provide inaccurate results. For example, GaN can present nitrogen deficiencies that depend on the analysis conditions (Saxey, 2011; Diercks et al., 2013). These deficiencies can range from 0 to $>90\%$ of the expected total nitrogen events. It has been proposed that neutral N₂ molecules can escape the

*Author for correspondence: Ty J. Prosa, E-mail: ty.prosa@ametek.com

Cite this article: Prosa TJ, Oltman E (2022) Study of LEAP® 5000 Deadtime and Precision via Silicon Pre-Sharpened-Microtip™ Standard Specimens. *Microsc Microanal* 28, 1019–1037. doi:10.1017/S143192762101206X

surface or disassociate from evaporated ions as neutral molecules under the right conditions (Saxey, 2011). This is an extreme example of analysis inaccuracy. Additional examples include oxides, like SiO₂, which commonly exhibit small deficiencies in oxygen not explained by the misidentification of overlapping O⁺ and O₂⁺⁺ ions (Kinno et al., 2014), and a number of atom types and features which seem more prone to correlated evaporation (De Geuser et al., 2007) than the rest of the periodic chart: carbon and carbides (Yao et al., 2010; Kitaguchi et al., 2014; Lewis et al., 2015; Thuvander et al., 2019), boron and borides (Menand & Kingham, 1984, 1985; Menand et al., 1984; Ronsheim et al., 2008; Larson et al., 2011; Meisenkothen et al., 2015, 2020b), iron (Rolander & Andren, 1989; Takahashi et al., 2011; Kitaguchi et al., 2014), and clusters (Marquis & Hyde, 2010). The possibility that different atoms or materials possess unique correlated evaporation properties will complicate any approach to universally correct for this phenomenon (Cerezo et al., 1984; Rolander & Andren, 1989; Rolander & Andren, 1994; Da Costa et al., 2012; Stephan et al., 2015; Hatzoglou et al., 2020).

In this study, we have utilized the closest thing to an analysis standard currently available for APT: the silicon pre-sharpened microtip (PSM) (Larson et al., 2013). This material is representative of the typical issues present in most well-behaved APT material application types and can be used to evaluate analysis protocols and corrections. These silicon tips possess several desirable qualities:

- Commercially available,
- Manufactured in lots of approximately hundred 36-tip coupons,
- Produced from a single ⟨100⟩-oriented Sb-doped high-purity wafer (single crystal),
- Tip heights and shapes are uniform,
- No FIB processing after etching, so no implanted impurities,
- Silicon isotopic abundances should not significantly fractionate within the wafer volume (Morishita & Satoh, 2004),
- Sb distributions expected to be uniform, consistent with extrinsic doping, and
- High analysis survivability under a large variety of acquisition conditions.

Materials and Methods

Instrumentation and Data Collection

Multiple LEAP® 5000 instruments (Local Electrode Atom Probe, CAMECA Instruments, Inc., USA) in both available platforms [reflectron (R) and straight (S)] were used to collect data for this study. Analysis conditions utilized variable laser-pulse energy (LPE) and variable detection rate (DR) to maintain a constant applied evaporation field [controlled by maintaining a constant Si⁺⁺/Si⁺ charge-state-ratio or CSR (Kellogg, 1982; Kingham, 1982)] and constant surface emission flux or ions-per-time-per-area (Prosa et al., 2013a). For example, maintaining a CSR = 30 and a detected flux of 0.5 ions/s/nm², with a laser-pulsing frequency of 200 kHz, requires an increasing applied LPE (~8–22 pJ) and DR [(~0.35–1.3% ions-per pulse)], as the applied voltage increased during acquisition (~4–9.5 kV) to maintain the targeted flux (Larson et al., 2013). CSRs of 1, 3, and 30 and detected fluxes of 1 or 0.5 ion/s/nm² were investigated in this study. For the R-platform, voltage-pulsed acquisition was also performed.

Non-default RHIT files (Larson et al., 2013) (proprietary, customized version of the default RHIT where default

prompt-ion-feedback filtering of multi-hit events was not performed (Kelly, 2011; Gilbert et al., 2014)) were converted by IVAS 3.8 (CAMECA Instruments, Inc., USA) to epos format files (Larson et al., 2013). Subsequent analysis of the multi-hit spectrum was performed by noncommercial software, the results of which are the subject of this paper and further described later.

Software was written to automate data processing procedures not available in commercial software. The key elements include an auto-ranging scheme, deadtime correction, and multi-hit field evaporation modeling.

Mass Spectrum Ranging

An *auto-range-width* scheme (each peak ranged based on its individual characteristics) was designed and evaluated against a *scaled-range-width* scheme (all peaks given ranges based on peak width of the dominant peak), with further description, evaluation, and comparison included in the Results and Discussion section. The ranging concepts embrace historical, simple continuous ranging definitions [min, max] for prospective peak positions (Miller, 2000), and utilizes adjacent (or very nearby) ranges to estimate background contributions to the peak range, a common method used in spectral analysis (Gedcke, 2001).

Two different ranging strategies were developed, each with ranging parameters that depend on the shape/width of the dominant peak: (1) Auto-range-width, and (2) scaled-range-width. Depending on the local background environment surrounding each peak, one of three types of background ranges were used to estimate the background contributions for each peak: (1) equivalent-width left-range, slightly off-set from the left edge of the peak's range limit, (2) adjacent ½-width ranges, and when sufficient space between peaks did not allow for ½-width ranges, (3) adjacent ¼-width ranges, requiring the background total to be doubled to compensate for the width differences. These ranging approaches do not fully account for peak overlaps, but prevent events of one peak being included in other peak via the background estimates.

The auto-range-width scheme takes prospective peak positions and assigns a minimum range width that grows until a termination criterion is reached. A minimum range specification is needed in case no statistically significant peak is detectable to enable reporting of statistically significant detection thresholds (Currie, 1968). The range-growth scheme increases the range size 2–4 mass histogram bins at a time, depending on the specific scheme. The range-growth direction (growth left, right, or symmetrical) is chosen to maintain an increase in net counts (ranged counts-background counts), and typically terminates when the net counts no longer increase (termination criteria are discussed in greater detail in a Results and Discussion section). This procedure allows for asymmetric ranges around the peak maximum, which is important for the non-gaussian peak shapes typical in APT, and reliably captures the statistically significant signal consistent with the results reported later in this paper. The scaled-range-width scheme takes a similar asymmetric centering approach, the peak width is predetermined based on the width of the dominant peak.

The goal in ranging is to define a quantitative procedure for setting range-bounds in place of qualitative, manual, and potentially biased range setting (Meisenkothen et al., 2020b). The validity of the current methods will be judged within the context of the results in this report. The primary aims being (1) ensure the maximum peak signal was captured while (2) maintain an accurate estimate of the underlying background which could originate

from out-of-time events, tails from neighboring peaks, or other artifacts (Prosa, 2018).

Deadtime Correction

The systematic loss of detected ions due to deadtime or pile-up becomes more statistically significant as dataset size grows. Consider a specimen where the probabilities that an emitted ion will hit the detector with mass-to-charge (m/z) within the i th range is known, P_i , and $\sum P_i = 1$. Regardless of the underlying multi-emission event statistics (relative amounts of correlated and random, Poisson emission), if one only considers multi-events of some multiplicity, then the proportion of each multi-event can be expressed as a function of P_i and the underlying detection efficiencies (Rolander & Andren, 1989). Considering emitted double event types M_{ij} and total emitted multi-event types N_i that describe the multi-emission,

$$M_{i<j} = M_{ij} + M_{ji} = 2N_2 P_i P_j \quad \text{and} \quad M_{ii} = N_2 P_i^2. \quad (1)$$

Of course a real APT detection system does not intercept the entire emission area from the specimen, has limited efficiency for any single ion (Vallerga & McPhate, 2000; Prosa et al., 2014), and has pile-up limitations for multi-events. Let c_k account for these various detection efficiencies that cause an emitted k -multi-ion to be detected as k' -multi-ion (ignoring pile-up for the moment). For example, emitted double events will necessarily have some probability of being detected as double (or single or empty) events, so detected (M' , primed = detected, unprimed = emitted) double events can be expressed as

$$M'_{i<j} = 2c_2 N_2 P_i P_j \left(1 + c_3 N_3 \sum_k P_k + c_4 N_4 \sum_{k,l} P_k P_l + \dots \right), \quad (2)$$

and the total number of detected double events becomes

$$N'_2 = \sum_{i,j \geq i} M'_{i<j}. \quad (3)$$

For a well-behaved APT system, where total observed multi-hit events are <10% of all events, the higher-order contributions for observed double events will be <10% and might be ignored without loss in predictive ability. This will be the case as we discuss the behavior of the silicon PSM.

The detector in the LEAP 5000 has a deadtime of <3-5 ns (Meisenkothen et al., 2015; Takahashi et al., 2011), so generally any events with $\Delta m/z \gtrsim 0.5$ Da (or impact sufficiently spatially separated on the detector) should not be strongly affected by deadtime. The implication is that multi-hit-statistics of ions with differing m/z are assumed to be significantly less affected by deadtime, and only multi-hit events where two ions of the same m/z hit the detector in nearly the same place are likely lost due to deadtime.

This simplification is important as M'_{ij} 's are then not affected by deadtime and can be used to estimate the missing M'_{ii} type events due to pile-up. Ignoring the contribution of higher-order multi-events being detected as double events and considering probability that two ions of the same m/z are detected as two events as a deadtime factor, f , which is the same for all ion types, then

$$M'_{i<j} \approx 2c_2 N_2 P_i P_j \quad \text{and} \quad M'_{ii} \approx f c_2 N_2 P_i^2. \quad (4)$$

These relationships can be arranged to eliminate all constants and variables except for the measured double events, M'_{ii} 's and M'_{ij} 's, and the deadtime factor using any subset of ranged peaks generally (and e.g. for three ion types):

$$\frac{2M'_{ii}}{f} \approx \frac{\prod_j M'_{i,j \neq i}}{\prod_{j \neq k} M'_{j \neq i,k \neq i}} \quad \left(\text{or} \right) \frac{M'_{ii}}{f} \approx \frac{M'_{ij} M'_{ik}}{2M'_{jk}}. \quad (5)$$

These predictions are not exact because of the statistical nature of the measurements, and for three or more peaks are overdetermined. The missing number of counts from pile-up, M'_{ii} , for three ion types can be estimated by fitting and solving for α :

$$M'_{ii} \approx \left(\frac{M'_{ij} M'_{ik}}{2M'_{jk}} - M'_{ii} \right) \approx \alpha P_i^2 \approx \alpha' P_i'^{2+\varepsilon}, \quad (6)$$

where α is a correction factor that could be estimated if the P_i 's were known. If instead one uses the detected, uncorrected peak fractions from the segment's full spectrum, P'_i , as an estimate for P_i , then the missing counts for all peaks can be estimated based on the uncorrected peak fractions from a subset of statistically significant peaks. A parameter, ε , improves the fitting by better approximating systematic differences in using P'_i as an estimate for P_i rather than an alternative; using an iterative approach where initial P'_i is replaced by the initial corrected values and repeated until convergence. It was found that a constant $\varepsilon = 0.1$ consistently provided the best χ^2 . Performing a χ^2 fit for the three missing ion type counts and solving for α yields:

$$\alpha' = (P'_1^{2+\varepsilon} + P'_2^{2+\varepsilon} + P'_3^{2+\varepsilon}) / \left(\frac{P'_1^{4+2\varepsilon}}{m_{11}} + \frac{P'_2^{4+2\varepsilon}}{m_{22}} + \frac{P'_3^{4+2\varepsilon}}{m_{33}} \right). \quad (7)$$

Once α' is determined, the missing counts for any peak can be estimated using Equation 6, providing corrections for all peaks in the spectrum.

For this study, the $^{28}\text{Si}^{++}$, $^{29}\text{Si}^{++}$, and $^{30}\text{Si}^{++}$ peaks were used to determine α' . These peaks were usually the three most intense, and for $\sim 10^7$ ion data subsets, the measured double-event counts for each pair-type were sufficient to provide meaningful precision. We note that estimated uncertainty in α' was typically 2–3% and these uncertainties were propagated through to final corrected compositions and isotope fraction uncertainties.

Multi-Hit Modeling

In a measurement, the true emission hit-statistics from a sample are transformed into experimentally detected hit-statistics, which may bear little resemblance to each other because of efficiency and deadtime effects. To better understand the true field evaporation nature of the samples, a parameterized model was developed to simulate the transformation from ion emission to detection in order to match experimental data. This exercise promotes improved understanding of both the natural field evaporation behavior of silicon in APT and detector performance.

A simple probabilistic, correlated field evaporation model with a limited number of parameters was developed. The three major silicon isotopes and two charge states were considered (six mass spectral peaks). The experimental data for model fitting then consisted of single-event (six types) and double-event counts

Table 1. Example Terms ($f=F$ for Simplicity).

Detected Event Type	Emitted	Detected	Equation
$^{28}\text{Si}^{++}$ Singles	Single	$^{28}\text{Si}^{++}$	$Dc'S (NAeP_{28}Q)$
	Double	$^{28}\text{Si}^{++}$	$(NAeP_{28}Q) [(Dc+Dc'S') (Ae'+A'e+A'e') + f' DcAeP_{28}Q]$
Total			$(NAeP_{28}Q) \{Dc'S + [(Dc+Dc'S) (1-Ae) + f' DcAeP_{28}Q]\}$
$^{28}\text{Si}^{++}-^{29}\text{Si}^+$ Doubles	Double	$^{28}\text{Si}^{++}-^{28}\text{SiH}^+$	$2N (Dc+Dc'S') AeP_{28}Q AeQ' P_{28}H$
	Double	$^{28}\text{Si}^{++}-^{29}\text{Si}^+$	$2N (Dc+Dc'S') AeP_{28}Q AeQ' P_{29}H'$
Total			$2N (Dc+Dc'S') (AeP_{28}Q AeQ')(P_{28}H + P_{29}H')$
$^{28}\text{Si}^{++}-^{28}\text{Si}^{++}$ Doubles	Double	$^{28}\text{Si}^{++}-^{28}\text{Si}^{++}$	$N (f Dc + Dc'S') (AeP_{28}Q AeP_{28}Q)$

(21 types since M_{ij} is not distinguishable from M_{ji}). As will be discussed later, the double-events were further divided into correlated, or events separated less than some critical distance, d , and uncorrelated, or separated greater than d . These count categories provide for 48 distinct pieces of information to be fit by the model.

The model consists of the following parameters:

- Total emitted events: $N = \sum_i N_i$
- Composition fraction: $P_{28}, P_{29}, P_{30} \rightarrow P_{28} + P_{29} + P_{30} = 1$
- Active area fraction: $A, A' \rightarrow$ probability A hits detector, A' does not, $A + A' = 1$
- Detection efficiency: $e, e' \rightarrow e$ detectable and e' not detectable
- Corr. versus Unc. factor: $Dc, Dc' \rightarrow Dc$ correlated and Dc' uncorrelated events

Six total degrees of freedom

Correlated Distribution (Dc):

- Deadtime +2 factor: $f, f' \rightarrow f M_{ii}$ type +2 events detected, $f' M_{ii}$ as single
- Deadtime +1 factor: $F, F' \rightarrow F M_{ii}$ type +1 events detected, $F' M_{ii}$ as single
- Charge-state (CS) fraction: $Q, Q' \rightarrow Q$ 2+ charge-state ions, $Q' 1+$ ions
- +1 CS hydride fraction: $H, H' \rightarrow H \text{ SiH}^+$ ions form, H' remain Si^+ ions

Four degrees of freedom

Uncorrelated Distribution (Dc'):

- Unc. Singles-emission frac.: $S, S' \rightarrow S$ singles and S' doubles
- CS fraction: $q, q' \rightarrow q$ 2+ charge-state ions, $q' 1+$ ions
- 1+ CS hydride fraction: $h, h' \rightarrow h \text{ SiH}^+$ ions form, h' remain Si^+ ions

Three degrees of freedom

Of particular interest in this study is the correlated evaporation behavior relative to uncorrelated or random evaporation behavior.

The model only considers ion-emission events that originate as single or double events, with the singles only coming from the uncorrelated part of the model, $Dc'S$. The double events originate from correlated events, Dc , plus uncorrelated events, $Dc'S'$, such that total events, $Dc + Dc'(S + S') = 1$. Overall, the described model provides 13 total degrees of freedom and 48 pieces of hit information for fitting. Some example terms are shown in Table 1. Minimization was performed using Minuit2 within the ROOT software library (Antcheva et al., 2009).

Fractional Concentration Error Propagation

In science, error estimates reflect two types of statistics: (1) descriptive, which describe or summarize the observed measurement of a system, and (2) inferential, which forecast future outcomes. In APT, Miller et al. has explained how Bernoulli trials can be used as a basis for understanding how to make inferential estimates for compositional variance of homogeneously composed materials (Miller, 2000):

$$\sigma_{c,c'} = \sqrt{\frac{cc'}{N}}, \quad (8)$$

where c is the fractional composition of some ion type, c' is the compositional fraction of the remainder ions (not c), and N is the total number of ions measured. The variance is symmetric in c and c' because changing the uncertainty in one affects the other (compositions are correlated).

Miller et al. also explain that this predictive variance is true regardless of the detection efficiency (for homogeneous or random composed materials). However, when one considers an ordered system, then the variance does depend on detection efficiency, e (Danoix et al., 2007a, 2007b):

$$\sigma_{c,c'} = \sqrt{\frac{cc'(1-e)}{N}}. \quad (9)$$

It is useful to note that this relationship also describes the descriptive statistics of an APT measurement; In the limit of perfect detection efficiency, all ions from a volume are detected, then there is no measurement error; however, this is not a useful description for assessing result equivalence, i.e. inferential statistics.

Take a perfectly ordered system like GaN, for example. For 100% detection efficiency, one would expect to get almost zero variance when comparing compositions for multiple sub-volumes. The variation of composition would only occur because of subtle variations in the volume boundaries which cause a few Ga or N ions to be unequally captured. In this special case, the detector efficiency would also be necessary to provide proper inferential statistics, while in almost every other circumstance, the efficiency does not play a role in predicting future outcomes.

The above relationships do not provide for a way to propagate errors from background contributions into net composition estimates; however, the same variance relationships can be derived from Normal counting statistics and error propagation. Consider two sets of ranges C and C' such that the number of measured events $N = N_C + N_{C'}$. The compositions then can be written as $c = N_C/(N_C + N_{C'})$ and $c' = N_{C'}/(N_C + N_{C'})$, clearly showing that compositions are correlated. Using error propagation, the variance becomes:

$$\sigma_c^2 = \sigma_{N_C}^2 \left(\frac{\partial c}{\partial N_C} \right)^2 + \sigma_{N_{C'}}^2 \left(\frac{\partial c}{\partial N_{C'}} \right)^2 = \sigma_{N_C}^2 \left(\frac{c'}{N} \right)^2 + \sigma_{N_{C'}}^2 \left(\frac{c}{N} \right)^2. \quad (10)$$

Using $\sigma_{N_C}^2 = N_C$, then

$$\sigma_c^2 = N_C \left(\frac{c'}{N} \right)^2 + N_{C'} \left(\frac{c}{N} \right)^2 = \frac{cc'^2}{N} + \frac{c'c^2}{N} = \frac{cc'}{N}. \quad (11)$$

Now consider ranges that estimate the background contribution for each ion range, B_C and $B_{C'}$, then $c = (N_C - B_C)/(N - B)$ and $\sigma_{N_C - B_C} = \sqrt{N_C + B_C}$. Following the same error propagation, the background corrected concentration variances becomes:

$$\begin{aligned} \sigma_{c,c'} &= \sqrt{\left(\frac{\sigma_{N_C - B_C}^2 c'^2 + \sigma_{N_{C'} - B_{C'}}^2 c^2}{(N - B)^2} \right)} \\ &= \sqrt{(N_C + B_C)(N_C - B_C)^2 + (N_{C'} + B_{C'})(N_{C'} - B_{C'})^2} / (N - B)^2. \end{aligned} \quad (12)$$

This expression simplifies back to the original Bernoulli expression by substituting zero for each of the background counts.

Results and Discussion

Best practices applied to a reliable characterization method should provide results that are self-consistent, with error estimates that accurately represent the statistical dispersion of the results from many measurements. In this study, we have collected many measurements from a standard material, assumed invariance in composition after processing for APT analysis, and used multiple LEAP instruments and analysis conditions to better understand the precision and accuracy of APT results. Since final composition results also depend on how the data is manipulated, data reduction practices are a critical part of this understanding as well.

The basis of this study is to use calculated isotopic abundances of the three silicon isotopes to evaluate APT performance. The advantage of having a large volume of data is that we can probe the statistics at almost any level of precision. For convenience,

we have broken data into ~10.5 million ion subsets. At this level of counting statistics, we show that imperfections in the raw data are evident such that the isotopic fractions disagree as a function of collection voltage, analysis condition, and instrument; however, after applying reasonable corrections for deadtime and background, good statistical agreement is achieved. Subsequently, results from small datasets can be combined to provide results with even higher levels of precision to assess even smaller levels of disagreement, or data reduction imperfections.

The results of this study are organized primarily in order of data reduction. Unfortunately, the effects of individual steps are convoluted and can only be evaluated via the final isotopic fraction results. Consequently, this section is organized to first describe and discuss each step of data reduction, holding the evaluation discussion for later when isotopic fractions are calculated from the full combination of auto-ranging, background and dead-time corrections as follows:

- All 29 datasets included in this study are generally described.
- Auto-range-width algorithm and adjacent-range background estimation are described and the resulting width determinations are reported.
 - These results are useful for later in the section when results of the auto-range-width algorithm are compared to data analyzed using a single scaled-range-width, providing some context for evaluating the sensitivity of isotopic fraction results as a consequence of ranging width decisions.
- Correlated evaporation is described and used to motivate the deadtime correction procedure described in the experimental section.
- Ranging, background, and deadtime corrections now allow determination of best practices and evaluation of the statistical description of the results is possible.
 - Auto-range-width and scaled-range-width both provide similar results with high precision, but the auto-range-width results are much more stable with parameter selection and may be more generally applicable to other systems.
- The multi-hit model described in the experimental section is used to predict the underlying evaporation behavior of the specimen, attempting to separate the pure field evaporation behavior from that of the detector filtered raw data.

Application of best practices data reduction shows all the ~10.5 million ion data subsets yield statistical agreement regardless of voltage, platform, or acquisitions condition (even voltage-pulse mode). It is only when data from each platform are pooled together (>1 billion ion datasets) to achieve the highest potential precision does statistical disagreement emerge. The results from each platform type shows a dispersion that is comparable to that predicted from propagation of the errors. The standard deviation of the results from the reflectron only differs marginally from the uncertainties estimated by counting statistics and error propagation. At the 10-ppm level of precision, the two platforms indicate slight disagreement in ^{28}Si isotopic fractions.

Collected Data Description

Over an 18-month period, several datasets were collected under constant field/CSR and detected flux conditions. Of these, a subset of 29 were included in this report: 26 laser-pulse mode, 13 each from R- and S-platforms, and each spread over five different

Table 2. Collected Data Summary.

Reference	Ions	MRP (FWThM)	PF	Vmax	Temp. (K)	CSR	Flux (ions/s/nm ²)	PSM
R01-01	50,094,188	418	200,000	10,089	50	30	0.50	C1-36
R01-02	66,381,472	424	200,000	10,590	50	30	0.50	C2-36
R01-03	114,179,089	389	200,000	10,591	50	30	0.50	C3-36
R01-04	249,933,995	368	200,000	15,000	50	30	0.50	C4-36
R01-05	76,727,911	418	200,000	10,582	50	30	0.50	C4-36
R01-06	118,618,416	378	312,500	12,600	50	10	0.94	C5-36
R01-07	81,153,349	389	200,000	10,989	50	30	1.00	C6-25
R02-08	46,243,914	406	200,000	9,618	50	30	0.50	C7-36
R02-09	297,034,831	346	200,000	15,000	50	30	0.50	C7-36
R02-10	237,812,197	431	200,000	12,536	50	3	0.50	C7-36
R03-11	64,196,183	400	200,000	10,020	50	30	0.50	C8-36
R04-12	75,201,294	406	250,000	10,564	50	30	0.63	C9-36
R05-13	71,889,235	424	200,000	9,571	50	30	1.00	C10-25
R01-01VP	52,244,651	201	200,000	10,086	50	NA	0.50	C1-36
R01-02VP	62,674,951	209	200,000	10,586	50	NA	0.50	C3-36
R02-03VP	34,976,531	199	200,000	9,617	50	NA	0.50	C7-36
S01-01	90,004,085	172	200,000	9,474	50	30	0.50	C11-36
S01-02	161,326,929	164	200,000	10,513	50	30	0.50	C11-36
S01-03	104,891,344	170	200,000	9,514	50	30	0.50	C11-36
S01-04	109,793,358	166	200,000	9,513	50	30	0.70	C11-36
S01-05	166,050,921	175	200,000	10,015	30	1	0.70	C11-36
S01-06	91,231,892	168	200,000	10,011	50	30	0.50	C11-36
S01-07	181,945,088	173	200,000	9,991	50	1	0.70	C11-36
S02-08	200,049,489	181	200,000	11,045	50	30	1.00	C12-25
S02-09	166,609,000	183	200,000	11,045	40	30	1.00	C12-25
S02-10	190,706,756	177	200,000	11,045	50	30	1.00	C12-25
S03-11	39,514,930	185	500,000	7,510	50	30	0.50	C13-36
S04-12	301,213,527	161	200,000	10,601	50	30	0.50	C14-36
S05-13	59,863,303	187	200,000	10,295	50	30	0.50	C15-36

reflectron and straight flight path instruments. In addition, three voltage-pulse mode datasets were collected from two different reflectron instruments as summarized in Table 2. Each dataset is referenced by configuration, instrument, and file number (e.g. R01-02VP is reflectron instrument #1, overall reflectron file #2 in voltage-pulse mode). Additional information includes MRP of the $^{28}\text{Si}^{++}$ peak at full-width-thousandth-maximum (FWThM), pulse frequency (PF), voltage of last acquired ion (V_{max}), temperature, CSR, acquisition flux, and coupon reference (PSM, e.g., C1-36 is coupon #1, 36-tip coupon type). Most of the data was collected at 200 kHz pulse frequency, 50 K base temperature, 30 $\text{Si}^{++}/\text{Si}^+$ CSR, 0.50 ions/s/nm², and using 36-tip PSM coupons, but there was some small variety in these conditions which are **bold** in the table. Typically, PSMs begin emitting ions by 2 kV and reach steady-state emission conditions by 2.5–3.5 kV. A newer style PSM with slightly longer and fewer tips per coupon (25 versus 36) was included in this study and separately noted in the table.

Auto-Ranging Results and Discussion

The first step in converting raw APT data into meaningful compositional results (or in this case isotopic fraction) is to assign counts to individual peak ranges (i.e., ranging) and provide an estimate of corrections to those counts (i.e., background estimation). Historically, manually defined, non-overlapping, continuous ranges [min, max] are defined for each observed peak (Miller, 2000). From an imaging perspective, this is a desirable approach because simple ion imaging also requires that each ion be assigned a single identity (and not, alternatively, an identity probability for example). Ranging based on manual, user-determined, arbitrary processes leads to issues in precision and accuracy as demonstrated by round-robin evaluations of results (Nakamura, 1986; Marquis et al., 2016). For this study, an auto-ranging algorithm is utilized to provide unbiased results, but just as importantly, to enable fully automated data processing of $>3.6 \times 10^9$ ions to assess the effects of each of

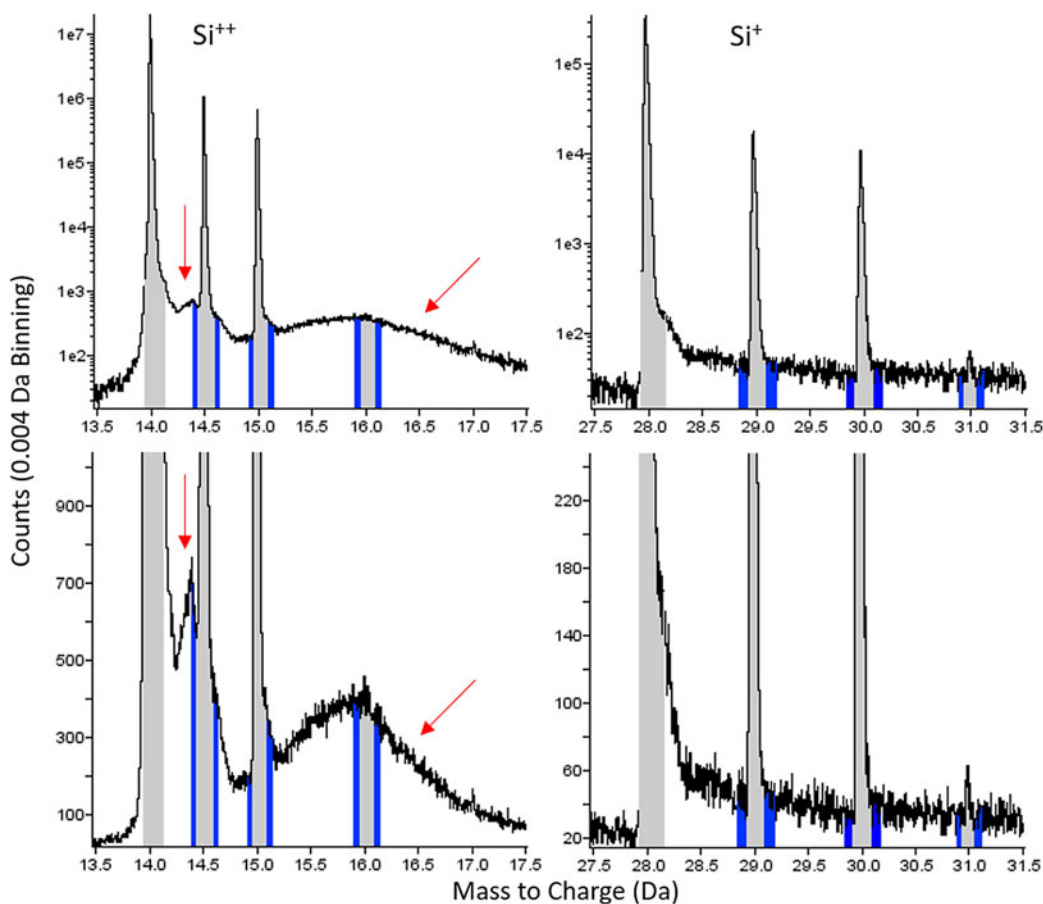


Fig. 1. Si^{++} (left, $\frac{1}{4}$ -width ranged) and Si^+ (right, $\frac{1}{2}$ -width ranged) regions of the mass spectrum from R01-07 consisting of $\sim 81 \times 10^6$ ions. The gray regions indicate the auto-determined peak range as described in the text. The blue regions are the adjacent $\frac{1}{4}$ -width or $\frac{1}{2}$ -width ranges used to estimate background contributions. Arrows in the figure indicate regions likely to contain ions produced from detection artifacts. The 16 Da region is a good example of ranging in search of an ion type (in this case O^+) that is near the detection threshold of the given dataset.

the data processing inputs (ranging, deadtime corrections, etc.) against the final results. Because of this requirement, background estimations available in commercial software could not be utilized and evaluated because of the fully automated processing requirement.

In developing a ranging strategy, common approaches including peak fitting and scaled range definitions were considered (Hudson et al., 2011; Haley et al., 2015; Meisenkothen et al., 2020b). Good precision (and accuracy) can be achieved when ranges capture equal peak fractions for all peaks, or alternatively, ranges are sufficiently wide to capture the entire signal while accurate assessment of the background mitigates the effects of overly broad ranging. Peak fitting would help for some of these challenges, but the literature provides limited solutions for mathematical peak shapes that can be used to systematically fit peaks in APT spectra (Johnson et al., 2013; Meisenkothen et al., 2020b). It seems the field evaporation physics works in such a way that the peak shapes vary from specimen-to-specimen, sometimes for different ion species, and shapes broaden as a function of m/z . Nevertheless, accurate ranging and background estimates are essential for precise measurements.

For the two ranging protocols described in the Experimental section, the background ranges are immediately adjacent to the peak-range under consideration. The widths of the background

ranges are either $\frac{1}{2}$ -current-peak-width or $\frac{1}{4}$ -current-peak-width, as part of both the auto-range-width determination and scaled-range-width range positioning. This type of background provides the mathematical equivalent of a linear background estimate, examples of which are shown in Figure 1. The $\frac{1}{2}$ -width method is preferred as it should provide better statistical estimates of the background, but there are other considerations. For example, the Si^{++} peaks (and 2+ peaks in general) are more closely spaced (more of an issue for S-platform data) and reside on a more complicated background shape (non-linear in many cases). This complexity is a result of the large number of ions in the region causing weak features to become statistically significant, including adjacent peak tails and detector artifacts (Gilbert et al., 2014) and is more compatible with the $\frac{1}{4}$ -width approach and an alternate auto-ranging-termination criterion which achieves generally better-looking fits. Note, the background ranges for ^{28}Si peaks are not shown in the figure, but utilize ranges of the same width, 1 Da to the left of those peak locations.

It is worth commenting that quantitative evaluation of ranging procedures is very important. Over the course of this investigation, it was found that this general termination scheme (termination by decrease in net signal) achieved statistically equivalent results, even for ranging that appeared non-optimum (worse looking by an experienced eye) and is part of the upcoming discussion.

Table 3. Ranging Descriptions.

Peak(s)	Range Method	Scaled-Width	Auto-Width Minimum	Auto-Width Stop Criteria
$^{28}\text{Si}^{++}$	Left-Side Full Range	$W \times \text{FWThM}$	NA	Width Set by W
$^{28}\text{Si}^+$	Left-Side Full Range	$1.2xW \times \text{FWThM}$	NA	Width Set by W
$^{29}\text{Si}^{++}, ^{30}\text{Si}^{++}$	Adj.-Sides 1/4-Range	$W \times \text{FWThM}$	$W/3x\text{FWThM}$	2nd Derivative
$^{29}\text{Si}^+, ^{30}\text{Si}^+$	Adj.-Sides 1/2-Range	$W \times \text{FWThM}$	$W/3x\text{FWThM}$	1st Derivative
Sb^{++}	Adj.-Sides 1/2-Range	$W \times \text{FWThM}$	$W/3x\text{FWThM}$	1st Derivative
Sb^+	Adj.-Sides 1/2-Range	$1.2xW \times \text{FWThM}$	$1.2xW/3x\text{FWThM}$	1st Derivative

Primary-Peak Scaled-Range-Width Ranging Criteria

The main (most intense) peak width (always the $^{28}\text{Si}^{++}$ in this study) was measured based on the mass spectrum for the entire dataset ($\sim 50\text{-}350 \times 10^6$ ions) at full-width-thousandth-maximum (FWThM). All prospective peak locations were then ranged starting with a minimum width based on the FWThM (important when a peak is extremely weak or nonexistent) and extending until a specific range termination criterion is reached. Because the ΔToF of the various peak widths is relatively constant, peak width in m/z increases with increasing m/z . Ranging parameter definitions were constructed to take this into account in a simple, limited way. A single width parameter, W , was used as a means to investigate how the ranging parameters affect final compositional results and provide information on the variation in range widths obtained by auto-ranging (variable width-sizing for all non- ^{28}Si peaks and for each dataset) for comparison with a scaled-width (fixed-width definitions based on measured $^{28}\text{Si}^{++}$ FWThM of each dataset) scheme as described in Table 3.

Auto-Width Ranging

The first derivative of the net counts function zero-crossing, (ranged counts-background estimate) < 0 , indicates a plateau in the net counts where statistical noise terminates ranging (causing zero-crossing). Too narrow a range will systematically undermeasure the net counts whereas too wide a range adds non-optimal background contributions, increasing the estimated uncertainty (decreasing precision). Overall, first-derivative crossing, with appropriate binning, tends to ensure accuracy with insignificant cost in precision.

The second derivative of the net counts function zero-crossing, (ranged counts-background estimate) < 0 , is useful when a peak resides on a broader peak in the background, and the first-derivative approach results in a range that captures both the main peak and the broader background peak beneath. This possibility occasionally occurred in the Si^{++} region of the mass spectrum and often when the background was not simply approximated by either flat, linear, or steadily decreasing background (peak resided in the tail of a lower- m/z peak).

A first derivative of the net counts function typically decays at a decreasing rate until reaching some maximum value. For a single peak residing on a broader background peak, the first derivative of the net counts function will have the same trend, but before reaching the plateau maximum, a discontinuity occurs where the background temporarily increases the first-derivative before decaying back towards some maximum value. Using the zero-crossing of the second derivative can work well in determining range-bounds for these datasets. For this study, first-derivative termination was used for all peaks except the Si^{++} peaks.

Spectral Binning

Binning schemes were evaluated over a range of 0.01–0.001 m/z widths. Conventional wisdom is that 10–20 bins should span the signal from the peak (Gedcke, 2005). This can be difficult to do in a single binning scheme for million-fold ranges in peak intensities. Ultimately, the most consistent results were achieved for a limited binning scheme, optimized more for the weaker peaks so that they would commonly have 10–20 bins for the statistically significant portion of the peak signal. The final binning formula in this study was based on both the total number of ions and FWThM of the main peak.

- Reflectron: 0.004 Da or 0.002 Da (for $>200,000,000$ ions)
- Straight: 0.008 Da or 0.004 Da (for $>200,000,000$ ions)

Auto-Width Ranging Results

The variability of ranging widths is illustrated in Figure 2 and Table 4 below for $W = 2.5$. The average peak widths for the R-platform are 2.3, 2.2, 2.4, and 2.4 (xFWThM) for the $^{29}\text{Si}^{++}$, $^{30}\text{Si}^{++}$, $^{29}\text{Si}^+$, $^{30}\text{Si}^+$ respectively with a standard deviation of $\sim 15\%$. In VP-mode the FWThM is broader with average scaled peak widths of 2.1, 1.9, 2.4, 1.5 respectively, and for the S-platform, 2.0, 2.4, 2.1, 2.1 respectively with a standard deviation perhaps slightly higher. Any apparent trends, like the Si^+ peaks being narrower for S relative to R in terms of scaled FWThM, are not very strong and difficult to rationalize. Considering these results (and others discussed later), a simple fixed, scaled-ranging scheme, utilizing a constant $W = 2.5$ (which approximately represents the maximum auto-ranged width here) works well capturing all the signal in this variety of datasets.

Multi-Hit Evaporation Correlations

Field evaporation correlations are very important in APT, enhancing some aspects of the technique while degrading others. For some crystalline materials or grains or particles, the somewhat ordered disassembly of the material allows for atomic planes to be resolved in reconstructed data, even in silicon (Prosa et al., 2013b). However, other aspects of nonrandom field evaporation are at the root of the composition disparities described in the introduction.

Poisson processes (in this case random in time and space) are useful because the occurrence of apparent coincident field evaporation (infrequent occurrence of multiple events during the same pulse or close together in space) can be mathematically predicted and thus corrected (Stephan et al., 2015). APT field evaporation, to a first approximation, has strong Poisson characteristics. For a



Fig. 2. Comparison of auto-range-widths. The ^{28}Si widths were set to be the same size for this comparison ($W=2.5$, so 2.5 and $3.0 \times \text{FWThM}$ for $^{28}\text{Si}^{++}$ and $^{28}\text{Si}^+$ respectively, **bold** in Table 4). Small scatter is observed in the ^{28}Si lines because range widths are required to be an integer number of bin widths, which may not exactly match the prescribed widths based on FWThM. The minimum widths for the remaining Si peaks are then set to $0.83 \times \text{FWThM}$ according to Table 3 (which do not affect auto-ranging here because of the peak strengths relative to background—all resulting widths \gg minimum width).

given average DR and detection efficiency, e , the proportion of double events to single events would be approximately $\sim e\text{DR}/2$, and triple events $\sim e^2\text{DR}^2/6$. Yet, significant non-Poisson correlations are present and have yet to be described in any predictable way.

We now describe the multi-hit evaporation behavior for silicon. The spatial correlations can be used to separate events into clearly Poisson-like (uncorrelated, multi-hit events) and strongly correlated events. As expected, the Poisson-like portion has larger separation and correlates with observed DR, while the correlated evaporation has a signature suggesting that atoms as far as 8–10 nm apart affect the probability of co-evaporation. The likelihood of correlated evaporation does not strongly depend on DR or how fast the material is disassembled but may only depend on analyzed volume. A difference in evaporation field (CSR) is apparent for correlated versus uncorrelated-evaporation events.

Figures 3 and 4 show the typical multi-hit evaporation exhibited by the samples in this study. The data histograms are in terms of number of double events (two hits detected during a single pulse) by reconstructed separation distance. Three data segments are plotted, from the same dataset, but represent three different average evaporation voltages corresponding to average ToF for the $^{28}\text{Si}^{++}$ ions of 1144, 985, and 823 ns respectively. This consideration is important as the deadtime will depend on ΔToF of events occurring during the same pulse. In addition, the double events are further separated into $^{28}\text{Si}^{++}$ -not $^{28}\text{Si}^{++}$ doubles (those likely unaffected by pile-up, ΔToF is always large, solid lines) and $^{28}\text{Si}^{++}$ - $^{28}\text{Si}^{++}$ doubles (those likely affected by pile-up, ΔToF is small, circles). The $^{28}\text{Si}^{++}$ -not $^{28}\text{Si}^{++}$ doubles have been scaled ($x8.1$) to account for differences in occurrence probabilities based on isotopic abundance considerations. In other words, for large separations (>8–10 nm) where deadtime should not occur, the plots should be similar when considering similar average ToF.

Uncorrelated-evaporation multi-hit events occur as a consequence of statistical correlations, predicted by the underlying Poisson statistics, both in time and space. All of the events observed with separations >10 nm have a distribution consistent with uncorrelated evaporation; most frequently, the separation is about half the detector diameter and it decays to zero toward the maximum separation (detector diameter) and zero because

of the homogeneous distribution of spatial pairs. Also, the number of events correlates with DR as expected (note all data were collected at constant flux, so the average DRs of 2.2, 4.0, and 8.2% would predict approximately 1.6, 2.9, and 5.8% $^{28}\text{Si}^{++}$ - $^{28}\text{Si}^{++}$. Things are different at small separations showing correlated field evaporation.

Figure 4 shows multi-hit evaporation events for doubles separated by <10 nm. The $^{28}\text{Si}^{++}$ -not $^{28}\text{Si}^{++}$ events show large numbers with an average separation of 2–3 nm. The numbers of these correlated events are larger than the number of uncorrelated evaporation events (6–7% of the total events) and not correlated with the 3× increase in DR. The deadtime issue is obvious in this plot comparison as almost no $^{28}\text{Si}^{++}$ - $^{28}\text{Si}^{++}$ events are observed (circles) relative to expectation based on $^{28}\text{Si}^{++}$ -not $^{28}\text{Si}^{++}$ (solid lines). If only a single event is detected when a correlated $^{28}\text{Si}^{++}$ - $^{28}\text{Si}^{++}$ event occurs, then 6–7% of all $^{28}\text{Si}^{++}$ events are missing relative to other isotopes and elements, independent of DR, so there is no simple way to minimize this effect by acquisition rate. Since silicon is considered a relatively well-behaved, correlated evaporation, APT material, this underlying behavior may be worse for applications with strong composition deficiencies.

Si Results: Deadtime Correction

Using the three Si⁺⁺-ranged peak correlations, the number of missing same–same double events was estimated by the procedure described in the Experimental section. Uncertainty of the deadtime based on the χ^2 fitting was propagated and included in the uncertainty of the composition results. The effectiveness of this procedure is first shown by improvement in the consistency of the isotopic fraction results as a function of acquisition voltage from single datasets, followed by the improvement in result consistency for similar acquisition voltages for all 29 datasets.

Figure 5 shows ^{28}Si -fraction results for datasets S02-10 and R02-09. Error bars indicate 2σ uncertainties, resulting from error propagation of the counting statistics and background subtraction. These analyses span >8 kV and 190×10^6 collected ions each, which afford the opportunity to evaluate results as a function of ToF and platform. The raw, S-platform results show a systematic $\sim 12\sigma$ variation as ToF decreases over the course of an

Table 4. Summary of Peak Widths Determined by Auto-Range-Width.

	FWThM (Da)	MRP	CSR	$^{28}\text{Si}^{++}$ (<i>W</i>)	$^{29}\text{Si}^{++}$	$^{30}\text{Si}^{++}$	$^{28}\text{Si}^+$	$^{29}\text{Si}^+$	$^{30}\text{Si}^+$
R01-01	0.067	418	32	2.51	2.15	2.87	2.99	2.39	2.27
R01-02	0.066	424	32	2.55	2.18	2.18	3.03	2.42	2.42
R01-03	0.072	389	32	2.56	2.44	2.22	3.00	2.78	3.11
R01-04	0.076	368	31	2.53	1.89	1.58	3.00	2.11	2.05
R01-05	0.067	418	31	2.51	3.10	2.39	2.99	2.39	2.75
R01-06	0.074	378	11	2.49	2.59	1.95	3.03	2.38	2.38
R01-07	0.072	389	30	2.56	2.22	2.00	3.00	2.33	2.33
R02-08	0.069	406	33	2.55	2.09	2.09	3.01	2.32	2.20
R02-09	0.081	346	31	2.52	1.58	1.58	3.01	1.93	1.78
R02-10	0.065	431	3	2.46	2.46	2.71	2.95	2.58	2.71
R03-11	0.07	400	32	2.51	2.29	2.74	2.97	2.51	2.51
R04-12	0.069	406	33	2.55	2.09	2.09	3.01	2.32	2.32
R05-13	0.066	424	32	2.55	2.67	2.67	3.03	2.42	2.18
Average	0.070	400		2.53	2.29	2.23	3.00	2.38	2.39
StDev	0.005	25		0.03	0.38	0.42	0.02	0.21	0.34
StDev			6%	1%	17%	19%	1%	9%	14%
<hr/>									
R01-01VP	0.139	201	4,171	2.53	2.30	2.07	2.99	2.19	1.61
R01-02VP	0.134	209	1,832	2.51	1.91	1.91	2.99	2.27	1.43
R02-03VP	0.141	199	3,845	2.50	2.04	1.82	2.95	2.84	1.48
Average	0.138	203		2.51	2.09	1.93	2.98	2.43	1.51
StDev	0.004	5		0.02	0.20	0.13	0.02	0.35	0.09
StDev			3%	1%	10%	7%	1%	15%	6%
<hr/>									
S01-01	0.163	172	31	2.45	1.96	2.36	3.04	1.87	2.06
S01-02	0.171	164	31	2.53	1.87	2.62	2.99	2.06	1.96
S01-03	0.165	170	32	2.52	1.94	2.72	3.01	2.04	1.94
S01-04	0.169	166	32	2.46	1.89	2.27	3.03	1.99	2.08
S01-05	0.16	175	1	2.50	1.80	2.40	3.00	2.70	2.80
S01-06	0.167	168	32	2.49	2.11	3.07	2.97	2.30	2.30
S01-07	0.162	173	1	2.47	1.78	2.37	2.96	2.47	2.77
S02-08	0.155	181	31	2.48	2.06	2.48	2.99	2.06	1.75
S02-09	0.153	183	32	2.51	2.09	2.72	3.03	2.20	1.78
S02-10	0.158	177	31	2.53	1.82	2.23	3.04	1.92	1.72
S03-11	0.151	185	32	2.54	3.18	1.91	2.97	1.91	2.01
S04-12	0.174	161	30	2.48	1.66	1.75	2.99	2.34	1.98
S05-13	0.15	187	32	2.45	2.13	2.13	2.99	1.71	2.03
Average	0.161	174		2.49	2.02	2.39	3.00	2.12	2.09
StDev	0.008	8		0.03	0.38	0.35	0.03	0.27	0.34
StDev			5%	1%	19%	15%	1%	13%	16%

acquisition. A smaller ($\sim 4\sigma$) variation is observed for R-platform data. A quantitative analysis of these results, relying on the indicated uncertainties, would conclude that the isotope fractions vary

with depth and that the two specimens have differing average isotope fractions at a very high confidence level, when in reality no isotope fractionation is believed to exist.

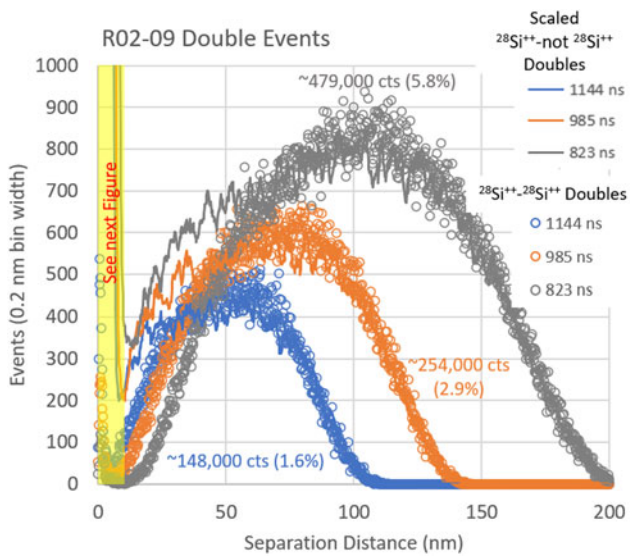


Fig. 3. Double-event separation histogram representative of typical Si PSM. $^{28}\text{Si}^{++}$ -not $^{28}\text{Si}^{++}$ events have been scaled, so that the probability of occurrence is equal to that of the $^{28}\text{Si}^{++}$ - $^{28}\text{Si}^{++}$ doubles. Three different voltage/ToF segments are plotted to show evolution of separation statistics during acquisition. The total number of events for separations >10 nm and the percentage of total events are displayed for each of the $^{28}\text{Si}^{++}$ - $^{28}\text{Si}^{++}$ plots.

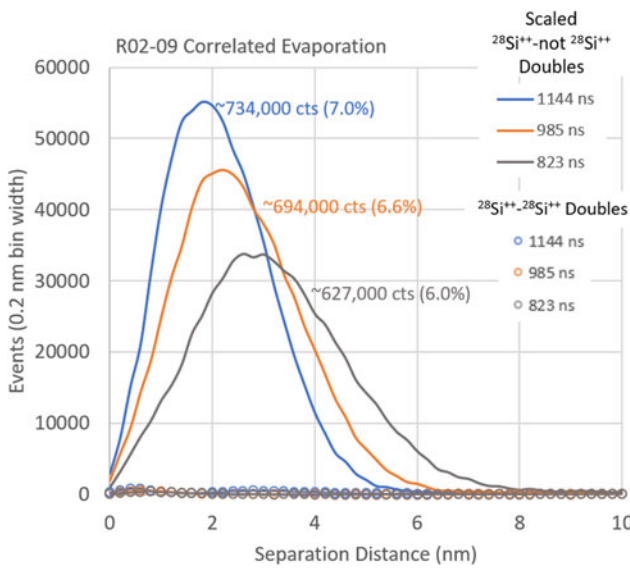


Fig. 4. Double-event separation histogram representative of typical Si PSM. $^{28}\text{Si}^{++}$ -not $^{28}\text{Si}^{++}$ events have been scaled, so that the probability of occurrence is equal to that of the $^{28}\text{Si}^{++}$ - $^{28}\text{Si}^{++}$ doubles. Three different voltage/ToF segments are plotted to show evolution of separation statistics during acquisition. The total number of events for separations <10 nm and the percentage of total events are displayed for each of the scaled $^{28}\text{Si}^{++}$ -not $^{28}\text{Si}^{++}$ plots.

Applying the simple deadtime correction described in the Experimental Section dramatically improves the statistical consistency of the results as shown by the corrected datapoints in Figure 5. The error bars are larger because the estimated deadtime uncertainty is $\sim 3\times$ larger than the counting statistics alone and included in the error propagation. This results in a $\sim 2\times$ increase in overall estimated uncertainty; however, the variation in ^{28}Si fraction as a function of ToF disappears, and the results between the two platforms now agree at a 95% confidence level. The

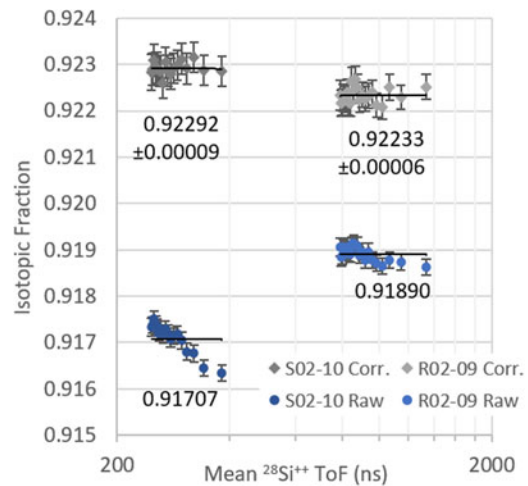


Fig. 5. ^{28}Si isotope fraction results for S02-10 and R02-09 datasets. Results are plotted as a function of the mean ToF for the ranged $^{28}\text{Si}^{++}$ ions, as deadtime effects should vary with ToF. The raw results are background corrected and the 2σ error bars are based on the propagation of counting statistics. The corrected results have been corrected for deadtime, and the 2σ error bars are based on counting statistics combined with the estimated error of the correction.

improved consistency in precision estimation is also seen when we compare data from similar ToFs, but for a variety of instruments and acquisition conditions.

Figure 6 shows the raw and deadtime-corrected ^{28}Si isotope fraction results for equivalent ToF subsets of data from each of 29 datasets summarized in Table 2 (note 3σ error estimates are plotted in this figure to improve visual clarity). In this case, for a single platform, similar analysis conditions (CSR), and similar ToFs, variation of the raw results (bar graph) is again consistent with the estimated precision, with only very small statistical disagreements at the 99% confidence level.

Larger variations are evident between platform, pulse mode (voltage versus laser), and analysis condition (CSR). Most of this variation can be explained by differences in CSR, or in other words, the distribution of detection probabilities for each of the six Si^+ and Si^{++} peaks. Deadtime effects are most prominent when the detection probabilities are most uneven (i.e., when the peak intensities are dominated by one or two strong peaks, see equation (1)), or in the case of silicon, predominantly occurring as $^{28}\text{Si}^{++}$ (larger CSRs). The raw data shows that ^{28}Si -fraction results increase inversely with CSR; voltage-pulse mode (>2000 CSR) provides the lowest computed fraction, and computed fraction increases as CSR decreases to 30, 10, 3, and 1. This represents a variation in $^{28}\text{Si}^{++}$ net signal from $\sim 91\%$ of the entire dataset down to $\sim 46\%$, resulting in computed ^{28}Si -fractions of 0.910–0.920 ($>100\sigma$ variation). There are smaller, but statistically significant platform differences as well ($\sim 15\sigma$).

For APT analysis without deadtime correction, the best statistically comparable results are obtained by using the same platform, similar, limited voltage range, same CSR, and relatively small datasets.

Figure 6 also shows the deadtime-corrected ^{28}Si isotope fractions. Ignoring the voltage-pulse mode results, all 26 of the laser-pulse datasets agree at a 99% confidence level, regardless of platform or acquisition condition. The voltage-pulse mode results differ by $\sim 7\sigma$, but this is a large improvement from results without deadtime correction and shows that the estimated precisions at least approximate the real precision of these measurements under the assumption that all measurements should yield the

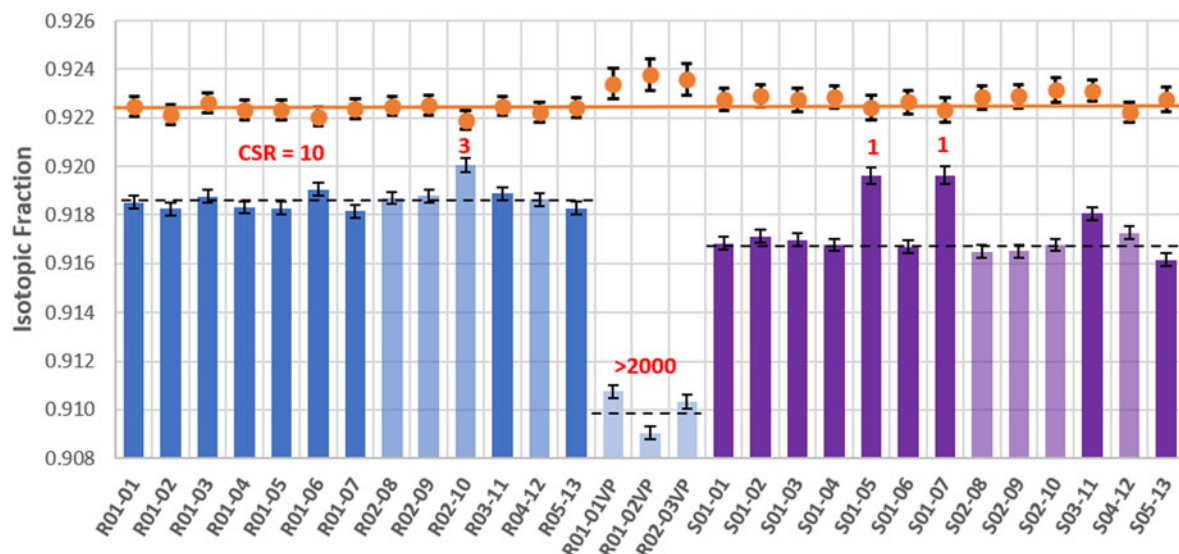


Fig. 6. ^{28}Si isotope fraction results of auto-range-width data. Each result is calculated from the $\sim 21\text{--}31.5 \times 10^6$ ion segment of the individual datasets described in Table 1. Because of the small, estimated error, 3σ error bars are shown. Bar plots represent raw data, while orange circles are the same data after deadtime correction. The seven datasets collected with CSR differing from 30 are indicated by red numbers.

same result. Pooling the 13 laser-pulse measurements for each platform improves the expected precision resulting in fraction estimates of 0.92233 ± 0.00041 and 0.92274 ± 0.00044 (3σ) for R- and S-platforms, respectively, indicating that a statistically significant difference remains between platforms using these precision estimates. Some possible explanations include an overestimation of the precision relative to the accuracy of the deadtime correction, systematic limitations of the deadtime correction relative to each platform type, or other unaccounted for factors important for large datasets. If these values are to agree, then the true uncertainty would need to be 3–6× greater than that estimated by the propagation of errors done here.

The ^{28}Si -fraction results from Figure 6 show how deadtime impacts results when a large fraction of the total events is concentrated in one or two peaks, but it is worth considering the impact on weaker peaks as well. Figure 7 shows the ^{30}Si -fraction results. Here, the raw data might appear to be in slightly better agreement, but the differences are still statistically large. In this case, the VP mode differs by $\sim 70\sigma$ to the laser-mode results, while R- and S-platforms differ by $\sim 13\sigma$, not so different from the ^{28}Si results. For the deadtime-corrected data, all laser-pulse data agree at 99% confidence level, with a similar, small disagreement for the voltage mode data as was the case for ^{28}Si .

The statistical agreement of all laser-mode data for dataset sizes of $>10^6$ ions suggests reasonable 1st order practices and corrections, but a more stringent test is to combine these equivalent datasets and to obtain results with higher precision. Figure 8 shows histograms of all 10.5×10^6 ion segments grouped by platform. The R- and S-platform result distributions are both quite good for the $>10^9$ ions represented here. The R-platform distribution appears Gaussian in shape and has a standard deviation that is only slightly broader than that predicted by error propagation, 0.00019 versus 0.00014. The S-platform distribution is not quite Gaussian with a standard deviation of 2× the predicted, 0.00035 versus 0.00017. At this level of precision, there is clear statistical disagreement from the two platforms, $>10\sigma$ difference. This disagreement could originate from the S-platform samples having some variation in the isotope fraction for the random PSMs

measured, or that the correction and ranging procedures are not good enough at this level for one or both of the platforms, or natural isotopic variation in silicon used as the source for wafer fabrication (Baskaran, 2012). The ability to compare these results to reliable measurements from another technique would help shed some light on these questions, and we hope to do this in the future. Table 5 summarizes the silicon isotope fraction results and compares the results to some accepted reference materials.

Si Results: Ranging Method Evaluation

Figure 9 shows the comparison of the two ranging methods described earlier. The parameter W has been varied in increments of 0.5, and the resulting ^{28}Si -fractions for the pooled data with the highest precision are included on the graph for auto-range-width and scaled-range-width methods.

The auto-range-width method results have less variability than scaled-range-width (see Table 4). This is because the only changes for the auto-range-width method, as a function of W , are the widths of the $^{28}\text{Si}^{++}$ and $^{28}\text{Si}^+$ peaks (only the minimum widths are affected by W for auto-range-width, which will be important for weak peaks or when prospective peaks are not detected and detection thresholds are calculated, not the focus of this report), while the scaled-range-width method changes the range dimensions for all peaks. The consequence for auto-range-width is that the wider the ^{28}Si range, the more the increase in its fraction contribution—to a point. Eventually, the additions become statistically insignificant as the fraction estimates plateau, even when the peak is effectively ranged to the border of the neighboring $^{29}\text{Si}^{++}$ peak (the maximum W values considered in the figure).

The evolution of the scaled-range-width method is more interesting. The fraction evolution of each platform suggests that the non- ^{28}Si peaks are under-ranged for $W < 2$. The adjacent-range background approach negatively distorts the net-count estimates when ranges are clearly too narrow, but they will still provide good estimates when over-ranged on a slowly smooth background. Ranging with $W < 2$ under-counts ^{28}Si -fraction (a problem), while

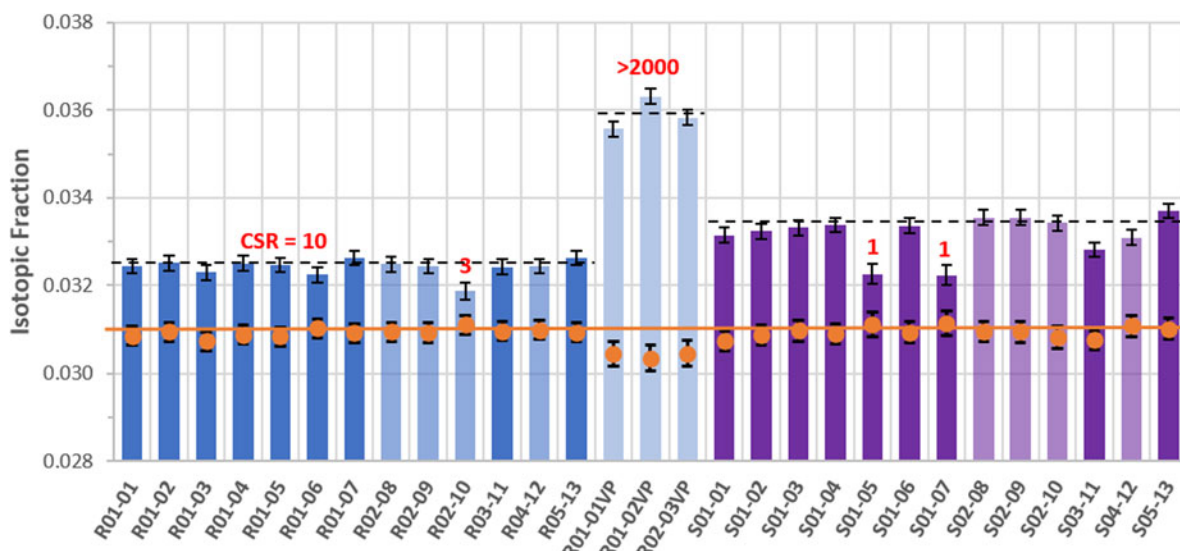


Fig. 7. ^{30}Si isotope fraction results of auto-range-width data. Each result is calculated from the $\sim 21\text{--}31.5 \times 10^6$ ion segment of the individual datasets described in Table 1. Because of the small, estimated error, 3σ error bars are shown. Bar plots represent raw data, while orange circles are the data after deadtime correction. The data collection CSR differing from 30 are indicated by red numbers.

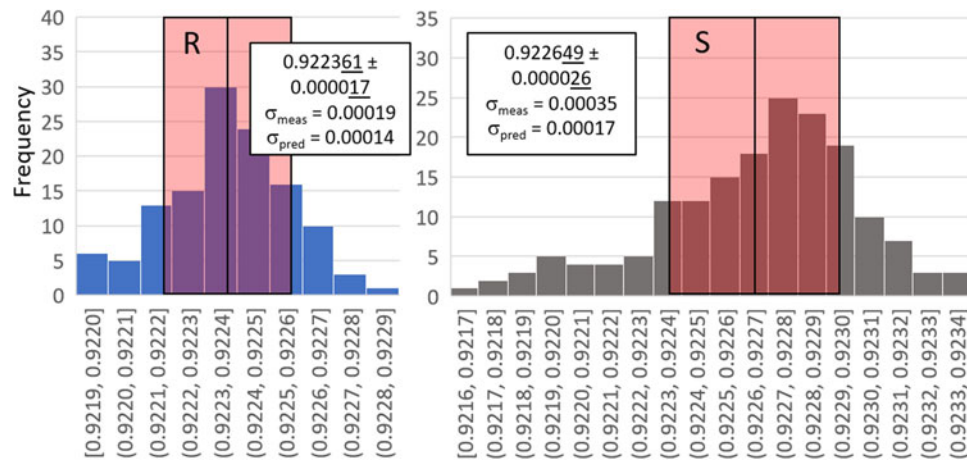


Fig. 8. Histogram of all laser-pulse, 10.5×10^6 ion segments ^{28}Si -fraction results grouped by the platform. The $\pm\sigma$ ranges about the mean are indicated by the red boxes. The isotope fraction ranges are indicated below each bin.

^{29}Si and ^{30}Si are over-ranged (not a problem). Because of peak-shape and background differences, the S-platform is much more sensitive to ranging width than the R-platform. It is notable that the two ranging methods agree for both platforms for W between 2 and 3. The S-platform gives the same results for W s of 2.5 and 3.0, while the R-platform results statistically agree over a range of 2–4 (the differences are less than 2σ). It is also notable that over this broad range of W , the estimated uncertainties do not change dramatically. The S-platform uncertainty estimates are larger for scaled-range-width, but the changes are more subtle than dramatic.

Based on these trends, the results included in the report utilize $W=2.5$ and auto-range-width methods as the automated approach promises to be the most flexible and adaptable for general application to other systems, and in this case for the Si-fraction measurements and ranging Sb dopants and other weak-peaked features in the datasets.

Sb Results

As described in Table 2, 15 distinct PSM coupons had tips analyzed as part of this study. Careful accounting was not done to track the specific lot of each coupon, so during the 18 months of this study, it is possible that coupons may have originated from different parent wafers and that these wafers may have come from different wafer lots. This fact does leave some room to expect that wafers cut from different bools may differ in average silicon isotopic abundance. Furthermore, the Sb-doping could also vary, even between coupons extracted from the same wafer. Nevertheless, the Sb composition measurements are available and show rather consistent average concentration suggesting a uniform dopant distribution over most coupons analyzed.

Figure 10 shows the results for Sb composition in ppm, from each of the 10.5×10^6 ion subsets, separated again by platform. These datasets, and further experience beyond those detailed in

Table 5. Silicon Isotopic Fraction Results by Platform with Additional Comparisons (2σ Uncertainty).

	^{28}Si	^{29}Si	^{30}Si
R-Platform	0.922361 ± 0.000034	0.046697 ± 0.000024	0.030943 ± 0.000016
S-Platform	0.922649 ± 0.000052	0.046435 ± 0.000040	0.030916 ± 0.000018
CIAAW Min. (Anon, n.d.)	0.92191	0.04645	0.03037
CIAAW Max. (Anon, n.d.)	0.92318	0.04699	0.03110
NBS-28 (Ding et al., 2005)	0.921751 ± 0.000028	0.046773 ± 0.000024	0.031474 ± 0.000014
IRMM-17 (Ding et al., 2005)	0.921821 ± 0.000033	0.046743 ± 0.000028	0.031435 ± 0.000017

this study, sometimes show increased Sb composition at the surface, so these histograms exclude measurements from the first 10.5×10^6 ion segments. In addition, each platform had an outlier dataset in terms of concentration trends: R04-12 and S05-13 were systematically high throughout (138 and 75 ppm average concentration) and excluded. The excluded measurements are shown in the zero-concentration part of the histogram. Although not plotted here, we note the R-VP mode results are similar with a composition of 36.9 ± 2.8 ppm with standard deviation of 8.3 ppm and expected uncertainty of 3.7 ppm.

These measurements of ppm composition show quite good agreement, even if the expectation of agreement is unknown because these wafers are specified in terms of resistivity and not composition, so some wafer-to-wafer variation is possible. Both platforms and R-VP mode results statistically agree at a 95% confidence level (after excluding the outliers). The R-platform distribution again quite closely matches that expected from propagation of errors, while the S-platform has a broader distribution. We note that the R-platform histogram contains results from nine different coupons, while the S-platform histogram contains results from only four. The S-platform distribution appears bi-modal and could describe two separate Sb distributions. A closer inspection of the data shows that the entire left peak in the S-platform distribution originates from C11 coupon, while the right comes from the remaining three coupons. Together, these results suggest that the Sb composition might be a reliable standard measurement for the PSM with caveats, especially if coupon origin/wafer lot is properly tracked by the manufacturer.

Overall, the ^{28}Si , ^{29}Si , ^{30}Si , and Sb results show the effects of deadtime on composition results. Because of the distribution of isotopic abundances, deadtime mainly affects ^{28}Si contributions, which are always underestimated relative to all other peaks. Figures 5–7 show that deadtime affects accuracy most significantly for ^{28}Si -fraction increase (relative to the estimated uncertainty), and less significantly, but still strongly for the smaller fraction peaks (^{30}Si). The weakest signal, the Sb composition, loses very little signal due to deadtime, so the composition is most affected by corrections of all the major peaks. For the data in this study, these major peak corrections result in a 3–13% relative reduction in the Sb composition, which is only a $\sim 1\sigma$ shift, whereas all the Si-isotope compositions/fractions shift by many σ as shown.

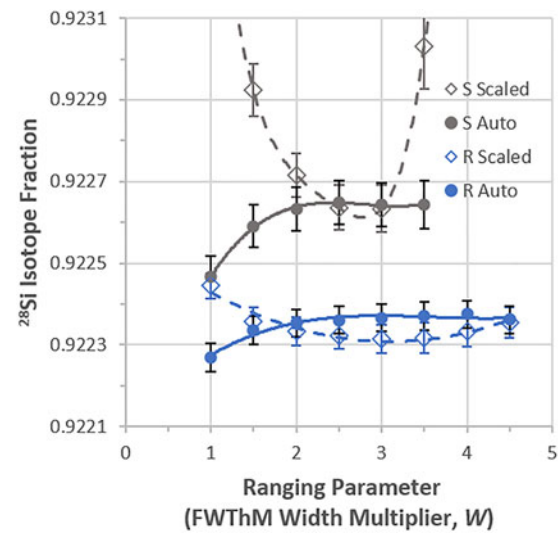


Fig. 9. Summary of ^{28}Si -fraction results as a function of automated-ranging parameter, W , utilizing all $\sim 10.5 \times 10^6$ ion segments. 2σ error bars are displayed. R- and S-platforms are indicated by the gray and blue curves, respectively. Auto-ranged and scaled-ranged results are indicated by solid and dashed curves, respectively.

Multi-Hit Modeling

The preceding data and discussions have illustrated some key features of field evaporation behavior for silicon. First, two categories of field evaporation are clearly present: correlated and uncorrelated. Correlated evaporation events are observable as pairs of ions departing during the same pulse at distances <8 nm from each other (ignoring the small overlap with the few uncorrelated ion pairs with separation <8 nm). There is no theory for predicting these event statistics. For pairs of ions of the same m/z range, most of these ions are only detectable as single events and are the dominant factor for deadtime deficiencies in ion counts. Uncorrelated events exhibit random correlations, consistent with those predicted by Poisson statistics, including an insignificant number of events at <8 nm spatial separation that would be impacted by detector deadtime. As shown in Figures 3 and 4, the number of multi-hit events from correlated evaporation is greater than those from uncorrelated evaporation, with the specific disparity dependent on DR. Second, Figure 5 shows that there are small, but significant, systematic deadtime variations over the course of an acquisition. In this section, the modeled field evaporation behavior, before interpretation by the detector, is reported, providing additional insights into the underlying statistical behavior of field evaporation decoupled from limitations imposed by the measurement.

Figure 11 is a plot of the fraction of correlated double events (D_c), relative to all evaporation events, versus the average ToF of the $^{28}\text{Si}^{++}$ ions as fit by the model. By plotting D_c as a function of ToF in log scale, the S- and R-platform datasets are visibly separated because of their non-overlapping ToF ranges (also indicated on the figure). Each of the 29 datasets is plotted with a unique color/symbol. Most of the datasets were collected with CSR = 30, but all the datasets are labeled by CSR to reveal clear trends. D_c does not change significantly over the course of an acquisition (even though the ER-DR change by large amounts during an acquisition), but D_c does depend on acquisition field. The D_c fraction ranges from 5, 6, 10, 13, and 40% for CSRs of 1, 3, 10, 30, and $>2,000$, respectively.

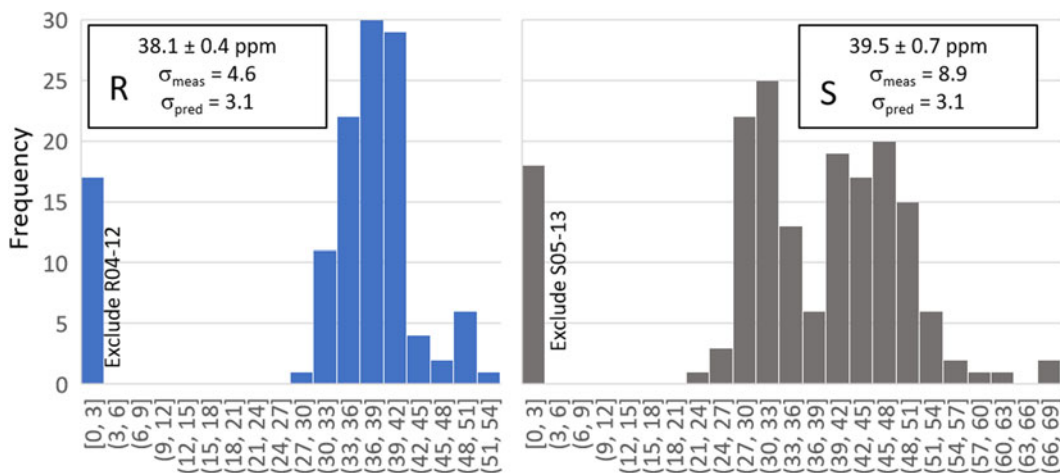


Fig. 10. Histogram of individual Sb composition results from all $\sim 10.5 \times 10^6$ ion segments (all compositions in figures are reported as ppm). A single outlier dataset from each platform was excluded as well as the first $\sim 10.5 \times 10^6$ ion segment from each dataset (see the text). Note histogram bin widths approximately equal the expected 1σ uncertainty based on the propagation of errors.

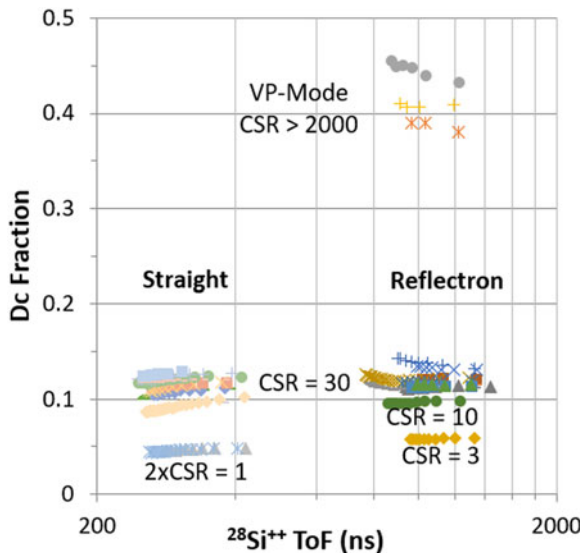


Fig. 11. Modeling results for estimated correlated doubles fraction, D_c , as a function of $^{28}\text{Si}^{++}$ average ToF for all data in the study. Note analysis order proceeds opposite ToF, so both analysis voltage and DR decrease from left to right.

Figures 12 shows plots of same m/z ion-pair detection probabilities, f and F , for the Si^{++} and Si^+ ions, respectively. It is important to note that there are many more multi-hit events recorded for the Si^{++} ions relative to the Si^+ ions because of the typical CSR used for acquisitions in this study, so the modeling results for F are of lower confidence. Nevertheless, the trends of both parameters are consistent. The difference in the two figures makes clear the major differences. Figure 12a plots both parameters in terms of the average ToF of the $^{28}\text{Si}^{++}$ ions. Here, the $\sim 50\times$ relative efficiency difference is clear (arrows). When the Si^+ detection probability, F , is plotted in terms of the average ToF of the $^{28}\text{Si}^+$ ions, Figure 12b, the pair detection probability appears to be approximately continuous with ToF. These trends are important to consider in instrument design (i.e., S-platform ions with ToF >500 ns might have very little deadtime and likewise for R-platform ions >2000 ns). However, the level of contribution

to observed deadtime variation with ToF is somewhat deceiving as will be discussed later.

Figure 13 shows that for long ToFs, some ability to detect Si^+ D_c events is possible (consistent with the model fits in Fig. 12b). Here, the first two 10.5×10^6 ion segments from the two CSR=1 datasets (S-platform) are plotted (chosen because they have the most Si^+ events in the entire study). The data from each equivalent segment have been combined to increase the number of events in each histogram bin. Contrasting with Figures 3 and 4, significant D_c events are observed in the <8 nm region. The average model fit values for F were 12.4 and 4.0% for segments 1 and 2, respectively. The 2nd segment shows a very small hint of an ability to detect correlated events when separations are >6 nm, and for higher numbered segments, no evidence of detected correlated events is observed (not shown).

Analysis DR appears to be the dominating factor for affecting deadtime losses, but the trend is opposite the expectation. Higher DR does provide for more multi-events (and deadtime losses) because of higher probability for random, Poisson correlations to occur (D_c' events); however, this increase is more than countered by the observed decrease in correlated evaporation events (D_c , the ones that dominate observed deadtime losses), resulting in decreased overall deadtime losses with increasing DR . Figure 14 plots the modeled fraction of events lost due to deadtime as a function of ToF and shows deadtime increasing with ToF. Since $^{28}\text{Si}^{++}$ - $^{28}\text{Si}^{++}$ detection probability, f , is very small, almost all D_c events are detected as single ions rather than double ions. Observed increases in f with longer ToF do increase deadtime with increasing ToF, but this is a minor effect because f remains small relative to DR effects. Analysis DR changes the fraction of D_c relative to D_c' events. Since analyses were performed under constant ions-per-area-per-time conditions, as analyses progress (decreasing ToF), the analysis DR increases to compensate for the increasing specimen emission area. Larger DR increases the fraction of D_c' and decreases the fraction of D_c , and this is reflected in the apparent loss of events at longer ToFs. An experiment conducted with constant DR would display a subtle and opposite trend.

In order to clarify the discussion, consider acquisition of a single-ion type where all emitted correlated double events

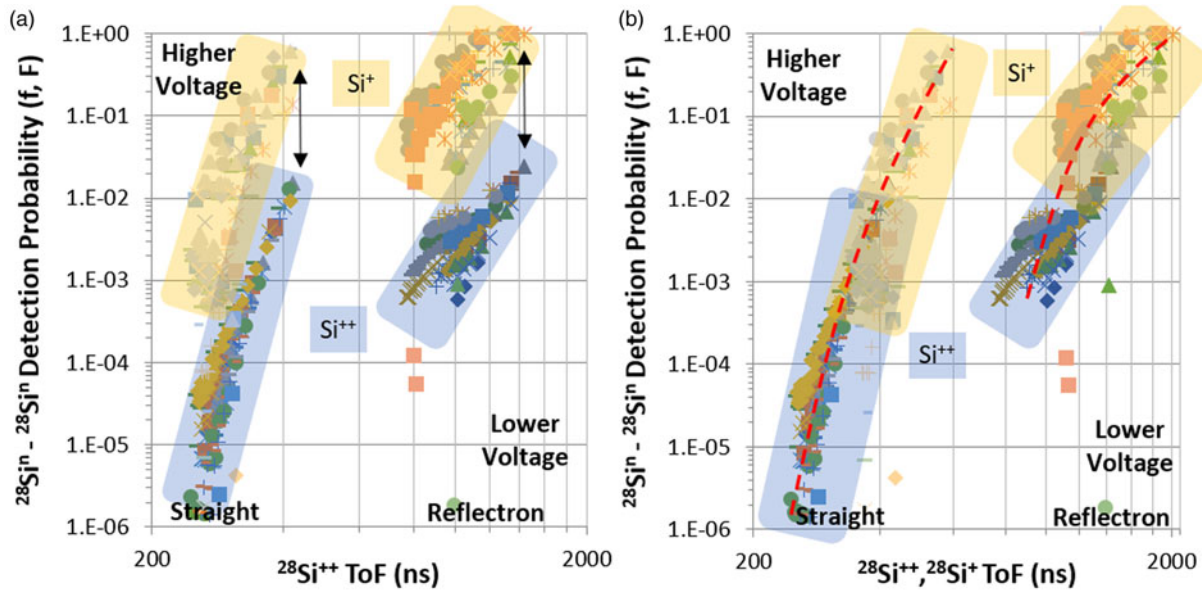


Fig. 12. Modeling results for the same m/z ion detection probability (deadtime factor). (a) The left figure plots all detection probabilities in terms of $^{28}\text{Si}^{++}$ average ToF. This highlights the $\sim 50\times$ better detection probability of Si^+ correlated ions relative to Si^{++} (arrows). (b) The right figure plots each ion factor type according to the average ToF of the ^{28}Si ion of that particular charge state. This highlights the approximately continuous evolution of f and F with ToF.

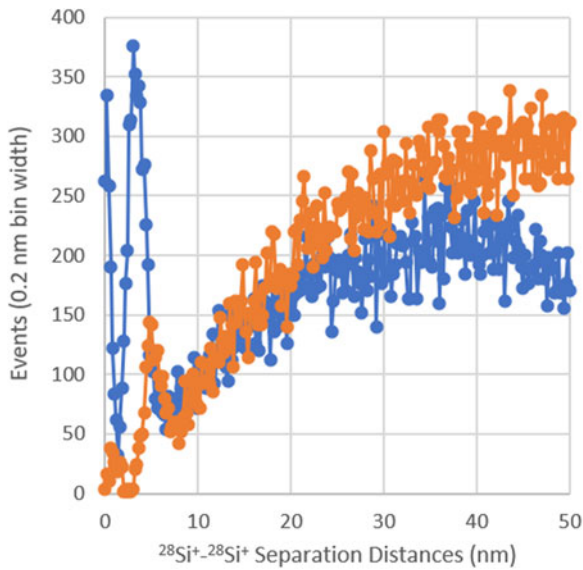


Fig. 13. Long ToFs on the S-platform show some ability to detect same m/z -ion events (voltages <5 kV). The blue and orange curves are plots of $^{28}\text{Si}^+-^{28}\text{Si}^+$ double events for the combined data from the two CSR=1 datasets, $\sim 10.5 \times 10^6$ ion segments 1 and 2, respectively. The blue curve shows some detected same m/z ion events missing in the orange curve.

(perhaps 10% of all emitted events) are detected as two events with efficiency f and single events with efficiency f' , and the remaining events (90%) are uncorrelated, Poisson distributed events without deadtime losses. The number of detected ions, N_{ions} , can be approximated as follows (see model definitions in the Experimental section):

$$N_{\text{ions}} = N\{[2ee'Dc + ee(1+f)Dc] + Dc'[eS + 2ee'(1-S) + 2ee(1-S)]\}. \quad (13)$$

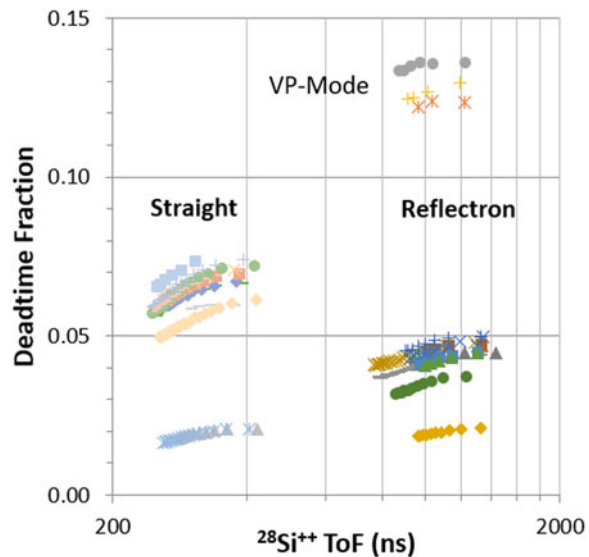


Fig. 14. Deadtime fraction (lost counts due to f and F) based on modeling results for all data in this study. The trends are consistent with those shown in Figure 5.

For a Poisson process, as mentioned previously, the ratio of double events to single events depends on the average emission rate, ER , as $(1-S)/S \approx ER/2$, leading to:

$$N_{\text{ions}} \approx eN\{Dc(1 + e' + ef) + Dc'/(1 - ER/2)\}. \quad (14)$$

The relative number of emitted correlated double ions, $2NDc/N_{\text{ions}}$, will depend on e , f , and ER (and f will depend on ToF as shown in the previous figures). For the variable ranges in this study, the effects of ER on deadtime are of 1st order importance, while f is so small the effects become lower order. Should f become similar in magnitude to ER , then both terms become important and deadtime trends could flatten or even invert and

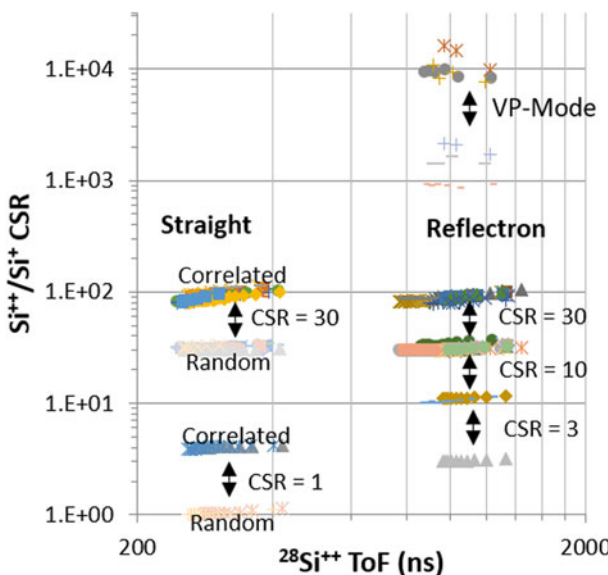


Fig. 15. Modeling results for charge-state fractions Q and q plotted as $\text{CSR} = Q/Q' = q/q'$ versus average $^{28}\text{Si}^{++}$ ToF. The correlated evaporation has a higher CSR and so the evaporation happens at higher field relative to the uncorrelated evaporation events. The $Q-q$ pairs of plots are indicated by the arrows. Almost all of the same CSR data provides the same fits (the data all plot on top of each other). Since there are typically more uncorrelated events, those CSR values match the experimental counterparts listed in Table 2.

decrease as a function of increasing ToF. When events are spread over multiple-ion peaks, the distribution of ion intensities with ToF will also become a factor for consideration. However, for this study, Equation 14 shows a decreasing number of D_c events with increasing ER which accounts for the decreasing deadtime loss with increasing ToF for constant flux acquisition.

Figure 15 shows the CSR for correlated and uncorrelated events separately (related to Q and q in the model). In all cases, the correlated events have a higher CSR than their uncorrelated counterparts. The difference corresponds to a $\sim 10\%$ higher field (Prosa et al., 2017). Perhaps, this suggests that spatial non-uniformities in evaporation allow periodic appearance of small, sharp features that eventually evaporate in a very quick, correlated manner once the local curvature can no longer resist field evaporation due to the local field enhancement. This relative sharpness may also provide a subtle magnification of correlated evaporation events relative to other events, consistent with the surprising large separation distances observed for these events (extending to 4–6 nm as shown in Fig. 4). Since PSMs are crystalline silicon all in the same orientation, one might expect to see an effect like this appear periodically in the reconstructed data as well; however, no clear spatial regularity in D_c was found.

Overall, the model is very useful for providing extra clarity regarding the field evaporation behavior of these silicon specimens. It is worth noting that a number of versions of this model were considered before the determination of the final version reported here. The multi-hit model evolved from a simple, single CSR distribution to the one described above in order to improve systematic misfits for various double events. Early observations suggested that two different CSR distributions were necessary to best represent the multi-hit information: high- and low-field distributions as shown in Figure 15. It was not until the data were arranged into correlated and uncorrelated information, and that the two different CSR distributions were associated with the correlated and

uncorrelated evaporation events. Because detector artifacts like ion feedback produce multi-events at some low level in all LEAP detectors (Gilbert et al., 2014), a modeling term to mimic this behavior, i.e., creating double events from single events, was considered. Ultimately, for these 10.5×10^6 ion datasets, the artifact was not prominent enough to be resolved independently of the other modeling parameters, except in a few exceptional circumstances, and so not included in the model used in this study.

General

The initial motivation for this study was to use the PSM standard to develop methods to better quantify P-doped silicon samples. The main challenge in this application is that high-yielding analysis conditions provide for significant Si^+ and P^+ ions, and under these conditions significant SiH^+ ions which creates a $^{30}\text{SiH}^+$ peak that directly overlaps with P^+ , complicating accurate dopant analysis. To precisely measure the P content, the P^+ and $^{30}\text{SiH}^+$ overlaps at 31 Da which must be accurately separated. *A priori* knowledge of the silicon isotope ratios can be used to estimate the overlap; however, this consideration prompted us to ask several questions including:

- What are the silicon isotope fractions for PSMs and do they vary by tip, coupon, or wafer?
- Are reported “natural abundance” values appropriate?
- Can APT measure the fractions and to what accuracy?

Natural isotopic abundance, of course, is some estimate of the Earth’s average isotopic abundances based on careful measurement of a few standard samples—one cannot possibly measure all the Si on Earth! Typically, isotope ratio measurements are performed in differential modes by comparing the measured isotope ratio of a set of samples to that of a standard (Brand et al., 2014). Secondary ion mass spectrometry (SIMS), for example, can be used and measuring ratios in differential modes causes some instrumental errors to cancel and avoids having to make absolute calibration of instrumentation. For silicon, the standard for comparison is NBS-28, which is an optical quartz, and a number of rocks and minerals from around the world contribute to the CIAAW range (Coplen & Shrestha, 2016). Table 5 shows some of the diversity in isotope fractions. Precision beyond three significant figures can become specific-material dependent.

Few APT studies have probed the accuracy and precision of the technique in detail (Prosa et al., 2013b; Meisenkothen et al., 2020a), but this study shows that it is possible to achieve very high precision on Si-isotope fractions. Extending the approach shown here to P-doped silicon, ideally analyzed at higher CSR, would allow one to make reliable measurement of the isotopic abundances for that sample from the Si^{++} ions (which do not exhibit hydrides) and use that information to decouple any overlaps at 31 Da.

Conclusions

This study has shown that PSMs are a good standard for Si-isotope fractions and Sb composition because they provide the same, precise results, regardless of instrument or analysis conditions, when consistent ranging, accurate background estimates, and deadtime corrections are used. Results yield precision consistent with error propagation, especially for the reflectron platform. Performing analyses under constant field/CSR and flux conditions is useful for decoupling the evaporation physics/statistics for

silicon PSMs, as each acquisition evolves only in terms of apex ion-emission area leaving local environments scaled in terms of field and emission rate. From the detection side, the extraction voltage always increases over the course of an analysis, so that the ToF of the ions (and ΔToF for pairs of ions) continuously decreases, potentially impacting the resulting detector performance (deadtime). Ideally, analysis conditions that keep the deadtime time-independent are desired. For bulk-like material systems, sufficient data on the multi-hit events can be collected to perform self-consistent deadtime corrections as demonstrated by this study. Constant field and DR acquisition may provide the most stable deadtime evolution with acquisition.

For data segments larger than $\sim 10^6$ ions, deadtime considerations and ranging become important for obtaining statistical agreement of measured compositions. Simple deadtime corrections and best practices produce Si-isotope fraction and Sb composition results with excellent statistical agreement for 10.5×10^6 ion datasets collected on various instruments, platforms, coupons, analysis conditions, analysis voltages, and laser- and voltage-pulse-modes. The estimated precisions based on counting statistics correlate very well with the standard deviation of the measurements. In the case of the R-platform, the standard deviation is less than 1.5 times the predicted uncertainty, while the S-platform is ~ 2 times the predicted uncertainty. The use of automated ranging, free of user bias, and adjacent background ranges enables the evaluation of large volumes of data for rigorous comparison of results for determining best practices. The ranging schemes utilized in this study, based on the FWThM of the $^{28}\text{Si}^{++}$ peak, show that precise, consistent results are obtained.

Multi-ion evaporation is the dominant factor for deadtime considerations, but detector performance based on average ToF also is a consideration. Both experimental data and modeling reveal consistent trends of multi-ion evaporation and deadtime depending on ToF, average evaporation field, and DR. The probability of detecting double events of the same ion isotope strongly depends on the ion ToF, platform, and the separation distance of the ions. The higher the average evaporation field, the greater the number of nonrandom, correlated evaporation events, and because these events arrive closely in space and time, this strongly affects losses due to deadtime. Finally, the correlated evaporation events occur at higher average field than the Poisson distributed evaporation events, even though the acquisition is controlled to have a constant average field/CSR.

References

- Anon (n.d.). CIAAW. Isotopic com position of the elements 2019. Available at www.ciaaw.org. [Online].
- Antcheva I, Ballintijn M, Bellenot B, Biskup M, Brun R, Buncic N, Canal P, Casadei D, Couet O, Fine V, Franco L, Ganis G, Gheata A, Gonzalez Maline D & Goto M (2009). ROOT — A C++ framework for petabyte data storage, statistical analysis and visualization. *Comput Phys Commun* **180**, 2499–2512.
- Baskaran M (Ed.) (2012). *Handbook of Environmental Isotope Geochemistry*. Berlin, Heidelberg: Springer-Verlag. Available at <https://www.springer.com/gp/book/9783642106361>.
- Brand WA, Coplen TB, Vogl J, Rosner M & Prohaska T (2014). Assessment of international reference materials for isotope-ratio analysis (IUPAC technical report). *Pure Appl Chem* **86**, 425–467.
- Cerezo A, Smith GDW & Waugh AR (1984). The FIM100 — performance of a commercial atom probe system. *J Phys C9*, 329–335.
- Coplen TB & Shrestha Y (2016). Isotope-abundance variations and atomic weights of selected elements: 2016 (IUPAC technical report). *Pure Appl Chem* **88**, 1203–1224.
- Currie LA (1968). Limits for qualitative detection and quantitative determination: Application to radiochemistry. *Anal Chem* **40**, 586–592.
- Da Costa G, Wang H, Duguay S, Bostel A, Blavette D & Deconihout B (2012). Advance in multi-hit detection and quantization in atom probe tomography. *Rev Sci Instrum* **83**, 123709.
- Danoix F, Grancher G, Bostel A & Blavette D (2007a). Standard deviations of composition measurements in atom probe analyses. Part I: Conventional 1D atom probe. *Ultramicroscopy* **107**, 734–738.
- Danoix F, Grancher G, Bostel A & Blavette D (2007b). Standard deviations of composition measurements in atom probe analyses—part II: 3D atom probe. *Ultramicroscopy* **107**, 739–743.
- De Geuser F, Gault B, Bostel A & Vurpillot F (2007). Correlated field evaporation as seen by atom probe tomography. *Surf Sci* **601**, 536–543.
- Diercks DR, Gorman BP, Kirchhofer R, Sanford N, Bertness K & Brubaker M (2013). Atom probe tomography evaporation behavior of C-axis GaN nanowires: Crystallographic, stoichiometric, and detection efficiency aspects. *J Appl Phys* **114**, 184903.
- Ding T, Wan D, Bai R, Zhang Z, Shen Y & Meng R (2005). Silicon isotope abundance ratios and atomic weights of NBS-28 and other reference materials. *Geochim Cosmochim Acta* **69**(23), 5487–5494.
- Exertier F, La Fontaine A, Corcoran C, Piazolo S, Belousova E, Peng Z, Gault B, Saxe DW, Fougerouse D, Reddy SM, Pedrazzini S, Bagot PAJ, Moody MP, Langelier B, Moser DE, Botton GA, Vogel F, Thompson GB, Blanchard PT, Chiaramonti AN, Reinhard DA, Rice KP, Schreiber DK, Kruska K, Wang J & Cairney JM (2018). Atom probe tomography analysis of the reference zircon gj-1: An interlaboratory study. *Chem Geol* **495**, 27–35.
- Gault B, Moody MP, Cairney JM & Ringer SP (2012). *Atom Probe Microscopy*. New York: Springer.
- Gedcke DA (2001). How Counting Statistics Controls Detection Limits and Peak Precision. *ORTEC Application Note AN59*.
- Gedcke DA (2005). How Histogramming and Counting Statistics Affect Peak Position Precision. *ORTEC Application Note AN58*.
- Gilbert JA, Gershman DJ, Gloeckler G, Lundgren RA, Zurbuchen TH, Orlando TM, McLain J & von Steiger R (2014). Invited article: Characterization of background sources in space-based time-of-flight mass spectrometers. *Rev Sci Instrum* **85**, 091301.
- Haley D, Choi P & Raabe D (2015). Guided mass spectrum labelling in atom probe tomography. *Ultramicroscopy* **159**, 338–345.
- Hatzoglou C, Rouland S, Radiguet B, Etienne A, Costa GD, Sauvage X, Pareige P & Vurpillot F (2020). Preferential evaporation in atom probe tomography: An analytical approach. *Microsc Microanal* **26**, 689–698.
- Hudson D, Smith GDW & Gault B (2011). Optimisation of mass ranging for atom probe microanalysis and application to the corrosion processes in Zr alloys. *Ultramicroscopy* **111**, 480–486.
- Johnson LJS, Thuvander M, Stiller K, Odén M & Hultman L (2013). Blind deconvolution of time-of-flight mass spectra from atom probe tomography. *Ultramicroscopy* **132**, 60–64.
- Kellogg GL (1982). Measurement of the charge state distribution of field evaporated ions: Evidence for post-ionization. *Surf Sci* **120**, 319–333.
- Kelly TF (2011). Kinetic-Energy discrimination for atom probe tomography. *Microsc Microanal* **17**, 1–14.
- Kingham DR (1982). The post-ionization of field evaporated ions: A theoretical explanation of multiple charge states. *Surf Sci* **116**, 273–301.
- Kinno T, Tomita M, Ohkubo T, Takeno S & Hono K (2014). Laser-assisted atom probe tomography of ^{18}O -enriched oxide thin film for quantitative analysis of oxygen. *Appl Surf Sci* **290**, 194–198.
- Kitaguchi HS, Lozano-Perez S & Moody MP (2014). Quantitative analysis of carbon in cementite using pulsed laser atom probe. *Ultramicroscopy* **147**, 51–60.
- Larson DJ, Prosa TJ, Lawrence D, Geiser BP, Jones CM & Kelly TF (2011). Atom probe tomography for microelectronics. In *Handbook of Instrumentation and Techniques for Semiconductor Nanostructure Characterization*, vol. 2, Haight R, Ross F & Hannon J (Eds.), pp. 407–477. London: World Scientific Publishing.
- Larson DJ, Prosa TJ, Ulfig RM, Geiser BP & Kelly TF (2013). *Local Electrode Atom Probe Tomography: A User's Guide*. New York: Springer.

- Lewis JB, Isheim D, Floss C & Seidman D** (2015). C13/C12-ratio determination in nanodiamonds by atom-probe tomography. *Ultramicroscopy* **159**, 248–254.
- Marquis EA, Araullo-Peters V, Etienne A, Fedotova S, Fujii K, Fukuya K, Kuleshova E, Legrand A, London A, Lozano-Perez S, Nagai Y, Nishida K, Radiguet B, Schreiber D, Soneda N, Thuvander M, Toyama T, Sefta F & Chou P** (2016). A round robin experiment: Analysis of solute clustering from atom probe tomography data. *Microsc Microanal* **22**, 666–667.
- Marquis EA & Hyde JM** (2010). Applications of atom-probe tomography to the characterisation of solute behaviour. *Mater Sci Eng R* **69**, 37–62.
- Meisenkothen F, McLean M, Kalish I, Samarov DV & Steel EB** (2020a). Atom probe mass spectrometry of uranium isotopic reference materials. *Anal Chem* **92**, 11388–11395.
- Meisenkothen F, Samarov DV, Kalish I & Steel EB** (2020b). Exploring the accuracy of isotopic analyses in atom probe mass spectrometry. *Ultramicroscopy* **216**, 113018.
- Meisenkothen F, Steel EB, Prosa TJ, Henry KT & Prakash Kolli R** (2015). Effects of detector dead-time on quantitative analyses involving boron and multi-hit detection events in atom probe tomography. *Ultramicroscopy* **159** (Pt 1), 101–111.
- Menand A, Al-Kassab T, Chambreland S & Sarrau JM** (1988). Atom-Probe study of aluminum-lithium alloys. *J Phys C* **6**, 353–358.
- Menand A & Kingham DR** (1984). Isotopic variations in field evaporation charge-state of boron ions. *J Phys D: Appl Phys* **17**, 203–208.
- Menand A & Kingham DR** (1985). Evidence for the quantum mechanical tunnelling of boron ions. *J Phys C* **18**, 4539–4547.
- Menand A, Martin C & Sarrau JM** (1984). Field evaporation charge state of boron ions: A temperature effect study. *J Phys* **45**, 95–98.
- Miller MK** (2000). *Atom Probe Tomography: Analysis at the Atomic Level*. New York: Kluwer Academic/Plenum Publishers.
- Miller MK & Forbes RG** (2014). *Atom-Probe Tomography: The Local Electrode Atom Probe*, 1st ed. Boston, MA: Springer US. Available at <http://link.springer.com/10.1007/978-1-4899-7430-3>.
- Morishita Y & Satoh H** (2004). Silicon isotopic zoning in silicon crystals caused by the isotopic fractionation at the crystal-melt interface. *Appl Surf Sci* **231–232**, 907–911.
- Müller EW** (1956). Field desorption. *Phys Rev* **102**, 618–624.
- Nakamura S** (1986). Round-Robin atom-probe experiment: Preliminary results in Japan. *J Phys* **47-C2**, 459–464.
- Prosa TJ** (2018). Understanding conditions affecting background in atom probe tomography with implications for analysis of hydrogen. *Microsc Microanal* **24**, 1028–1029.
- Prosa TJ, Geiser BP, Lawrence D, Olson D & Larson DJ** (2014). Developing detection efficiency standards for atom probe tomography. *SPIE Proc* **9173**, 917307.
- Prosa TJ & Larson DJ** (2017). Modern focused-Ion-beam-based site-specific specimen preparation for atom probe tomography. *Microsc Microanal* **23**, 194–209.
- Prosa TJ, Lenz DR, Payne TR, Oltman E, Bunton JH, Ulfig RM & Larson DJ** (2013a). Novel evaporation control concepts. In *Frontiers of Characterization and Metrology for Nanoelectronics*, Secula EM & Seiler DG (Eds.), , pp. 269–272. Gaithersburg, MD: NIST.
- Prosa TJ, Olson D, Geiser B, Larson DJ, Henry K & Steel E** (2013b). Analysis of implanted silicon dopant profiles. *Ultramicroscopy* **132**, 179–185.
- Prosa TJ, Reinhard DA, Francois-Saint-Cyr HG, Martin I, Rice KP, Chen Y & Larson DJ** (2017). Evolution of atom probe data collection toward optimized and fully automated acquisition. *Microsc Microanal* **23**, 616–617.
- Rolander U & Andren H-O** (1989). Statistical correction for pile-up in the atom-probe detector system. *Coll Phys* **50**, 529–534.
- Rolander U & Andren H-O** (1994). Study of proper conditions for quantitative atom-probe analysis. *Appl Surf Sci* **76–77**, 392–402.
- Ronsheim P, Flaitz P, Hatzistergos M, Molella C, Thompson K & Alvis R** (2008). Impurity measurements in silicon with D-SIMS and atom probe tomography. *Appl Surf Sci* **255**, 1547–1550.
- Saxey DW** (2011). Correlated ion analysis and the interpretation of atom probe mass spectra. *Ultramicroscopy* **111**, 473–479.
- Stephan T, Heck PR, Isheim D & Lewis JB** (2015). Correction of dead time effects in laser-induced desorption time-of-flight mass spectrometry: Applications in atom probe tomography. *Int J Mass Spectrom* **379**, 46–51.
- Takahashi J, Kawakami K & Kobayashia Y** (2011). Quantitative analysis of carbon content in cementite in steel by atom probe tomography. *Ultramicroscopy* **111**, 1233–1238.
- Thuvander M, Shinde D, Rehan A, Ejnermark S & Stiller K** (2019). Improving compositional accuracy in APT analysis of carbides using a decreased detection efficiency. *Microsc Microanal* **25**, 454–461.
- Tsong TT, Ng YS & Krishnaswamy SV** (1978). Quantification of atom-probe FIM data and an application to the investigation of surface segregation of alloys. *Appl Phys Lett* **32**, 778–780.
- Vallerga JV & McPhate JB** (2000). Optimization of the readout electronics for microchannel plate delay line anodes. In *Instrumentation for UV/EUV Astronomy and Solar Missions*, vol. 4139, Fineschi S, Korendyke CM, Siegmund OHW & Woodgate BE (Eds.), pp. 34–42. International Society for Optics and Photonics. Available at <https://www.spiedigitallibrary.org/conference-proceedings-of-spie/4139/0000/Optimization-of-the-readout-electronics-for-microchannel-plate-delay-line/10.1117/12.410543.short>.
- Yao L, Gault B, Cairney JM & Ringer SP** (2010). On the multiplicity of field evaporation events in atom probe: A new dimension to the analysis of mass spectra. *Philos Mag Lett* **90**, 121–129.